Computational Mechanics
https://doi.org/10.1007/s00466-023-02398-5

ORIGINAL PAPER

A finite element implementation of finite deformation surface and bulk poroelasticity

Jaemin Kim[1] · Ida Ang[1] · Francesco Ballarin[4] · Chung-Yuen Hui[1,2,3] · Nikolaos Bouklas[1,2]

Received: 16 May 2023 / Accepted: 15 September 2023

Abstract
We present a theoretical and computational model for the behavior of a porous solid undergoing two interdep
the finite deformation of a solid and species migration through the solid, which are distinct in bulk and on sur
theories allow us to systematically study porous solids in a wide range of applications, such as drug delivery, biomaterial
design, fundamental study of biomechanics and mechanobiology, and the design of sensors and actuators. As we aim to
understand the physical phenomena at a smaller length scale, towards comprehending fundamental biologic
miniaturization of devices, surface effect becomes more pertinent. Although existing methodologies provide
tools to study coupled bulk effects for deformation and diffusion, however, little is known about fully coupled bulk
and surface poroelasticity at finite strain. Here we develop a thermodynamically consistent formulation for su
poroelasticity, specialized for soft hydrated solids, along with a corresponding finite element implementation
three-field weak form. Our approach captures the interplay between competing multiphysical processes of m
and species diffusion, accounting for surface kinematics and surface transport, and provides invaluable insigh
effects are important.

Keywords Surface diffusion · Surface energy · Hydrogels

1 Introduction

Poroelasticity is the theory that describes the coupling of deformations of a continuum body with diffusive flow of a solvent through the body itself due to its permeable porous nature. The theory of linear poroelasticity as pioneered by Biot [8–10] has been applied to describe hydrogels and hydrated biological tissues [3,40], but in many cases nonlinear variants of the theory of poroelasticity are necessary due to bulk deformation of finite deformations and nonlinear complex constitutive responses [12, 13, 16, 42, 59]. These nonlinear theories have been highly relevant in the past few decades as the study of hydrated biomaterials and soft tissues and hydrogels at finite strains. Applications in drug delivery, tissue regeneration, biomaterials design, fundamental studies in biomechanics and mechanobiology, and design of morphing structures as well as sensors and actuators, nonlinear theories of poroelasticity have provided a deeper understanding of the rich observed material and structural responses. However, the majority of these studies have been in the macroscale, where surface effect can often be neglected as bulk energetic contributions dominate the response of the system. But, as we aim towards miniaturization of devices and also aim to probe and fundamentally understand the effects that dominate the material response at smaller length scales surface effect become more relevant. When the length scales that are probed are sufficiently small, one can expect the coupling of elasticity and solvent diffusion to be significantly influenced by surface contributions toward all aspects of these multiphysical processes.

Following free energy-based phenomenological approaches for the bulk response of materials, similar

B Nikolaos Bouklas
nb589@cornell.edu

1 Sibley School of Mechanical and Aerospace Engineering, Cornell University, Ithaca, NY 14853, USA

2 Field of Theoretical and Applied Mechanics, Cornell University, Ithaca, NY 14853, USA

3 Global Station for Soft Matter, GI-CoRE, Hokkaido University, Sapporo, Japan

4 Dipartimento di Matematica e Fisica “N. Tartaglia”, Universita` Cattolica del Sacro Cuore, Via della Garzetta 48, 25133 Brescia, Italy

Published online: 14 October 2023

approaches can be developed to study the surface and interface response of materials and material systems. The pioneering works of Gurtin [25, 26] established a systematic framework to derive kinematics and balance principles for surfaces that focused on the thermodynamics of purely elastic systems. Further, this framework was extended by Gurtin to account for thermal effects and mass transport, particularized for surfaces [24]. Many studies have followed since exploring the mechanics of surfaces and interfaces for continua involving purely mechanical as well as coupled processes [18, 28, 37, 44, 54].

The competition of bulk and surface energetics is length scale dependent. For elastic solids with shear modulus G and surface energy γ, the relevant length scale is the elastocapillary length $\ell = \gamma/G$ [55]. Generally speaking, if the characteristic dimension is much larger than elastocapillary length ($H \gg \ell$), surface effects are negligible. On the other hand, if the characteristic dimension is much smaller than elastocapillary length ($H \ll \ell$), surface effects are dominant. Focusing on soft solids, work from Style et al. [55] and Bico et al. [7] focused on the implication of surface energetics on the mechanical behavior of this class of materials, looking at the subtle relationships between surface response and the bulk response. Surface and interface energetics have been further explored in the context of soft solids to study their implications to adhesion, fracture, instabilities as well as the design of composites.

Specialized boundary value problems allow for the development of analytical solutions in this context [2, 12]. However, finite element implementation that accounts for surface effects is necessary to tackle general problems. Notably, Javili and Steinmann [34] developed the finite element framework for finite deformation accounting for surface energetics. Steinmann and co-authors [36, 50] also developed finite element schemes to study several classes of coupled problems, including mass transport and thermomechanics. These types of frameworks allowed the study of morphogenesis and wound healing in microtissue systems, where "active" surface and bulk effects were shown to emanate from the cellular activity of the extracellular matrix [38, 39, 49]. Focused on drug delivery applications, Boukamel and co-authors [2] investigated the mechanical surface effects in the context of finite deformation poroelasticity, uncovering the importance of such effects on the transient response of swelling hydrogel microspheres of the porous solids coupled with solvent diffusion using a mixed finite element method. More recently, Dortdivanlioglu and co-authors [52] proposed a computational formulation that allows the consideration of curvature-dependent surface energies using isogeometric analysis.

There is an extensive body of work on the development of mixed finite element frameworks for linear poroelasticity, including stabilization approaches for the treatment of numerical instabilities that are known to arise due to the violation of the Ladyzhenskaya-Babuška-Brezzi (LBB) condition [3, 6, 14, 51]. For different variants of nonlinear poroelasticity, an array of approaches has been proposed [2, 13, 16, 17, 20, 31, 41, 47, 48, 60]. Although the existing methodologies provide the necessary tools to study coupled bulk effects for deformation and diffusion, to the best of the authors' knowledge an implementation of the finite element framework that fully couples bulk and surface poroelasticity under finite strain has not been previously presented. Motivated by the theoretical work of McBride et al. [40], who considered coupled thermomechanics with species diffusion accounting for individual surface energetic contributions from elasticity, heat transfer and mass diffusion, here we aim to develop a robust and open-source finite element framework for the treatment of surface and bulk poroelasticity. In our previous work [2], we considered the surface elasticity coupled with poroelasticity in bulk, not accounting for surface diffusion.

The ultimate goal of this paper is the development of a thermodynamically-consistent formulation for surface and bulk poroelasticity specialized for soft hydrated solids, along with the development of a corresponding finite element implementation. Focusing on soft solids, and more specifically hydrogels, we discover a set of numerical complications that are not evident when the general theoretical framework is presented. This is because of the nature of the coupling of surface and bulk poroelasticity, as well as the nearly incompressibility assumption utilized to model the elastomeric component of the hydrogel. The manuscript is organized as follows: In Sect. 2, we describe the coupled theory, including kinematics, balance laws and the general form of the constitutive equations considering both bulk and surface energetics. In Sect. 3, the free energies are specialized for a hydrogel material. Section 4 presents the finite element implementation including the weak form, normalization and solution procedure. Section 5 elaborates on the numerical simulations for two three-dimensional (3D) boundary value problems corresponding to free-standing response of a cube as surface effects dominate, as well as the response under external loading highlighting unique contributions of surface effects, and the bulk and surface diffusion effects. Section 6 provides the conclusions and outlook for future work.

2 A continuum multiphysics approach for bulk and surface poroelasticity

In this section, we present a brief overview of key concepts of differential geometry towards describing the kinematics, mechanical equilibrium and mass balance, and obtain the constitutive relationships for the constitutive relations for the bulk and surface responses. It is noteworthy that a surface qua

tity to be introduced is not necessarily the same as the bulk quantity evaluated on the surface. Let V be a fixed reference configuration of a continuum body B, where material points in the reference configuration are tracked through the vector $X \in V$.

Remark 1 (Notation) The dyad ($\otimes$) and dot ($\cdot$) denote the tensor and dot products, respectively. The double dot ($:$) denotes the double contraction over two second-order tensors; e.g. $A : B = A_{ij} B_{ij}$. For convenience, we adopt the convention that other operations involving repeated indices will not be indicated by a specific symbol, specifically meaning for $v = Au$ ($v_i = A_{ij} u_j$) and $A = BC$ ($A_{ij} = B_{ik} C_{kj}$), we do not write $v = A \cdot u$ and $A = B \cdot C$, respectively. Throughout the text, we use the Einstein summation convention: when an index variable appears twice in an expression, it implies summation of that variable over all values of the index. Latin indices take the value 1, 2, 3, and are used in variables describing the ambient, three-dimensional, Euclidean space. Greek indices take the value 1, 2, and are used in variables in the embedded, two-dimensional, surface. $\{\cdot\}$ and $\{\breve{\cdot}\}$ denote bulk and surface quantities, respectively, for a body occupying volume V bounded by outer surface denoted as S. The overhat $\{\breve{\cdot}\}$ denotes normalized quantities, and the superposed dot $\dot{\{\cdot\}}$ denotes the material time derivative. We write $A^{-1} = (A)^{-1}$ and $\mathrm{tr}(A)$ for the inverse and trace of a tensor A. The double-bracket ($[\![\breve{\cdot}]\!]$) represents the average and jump of a surface quantity ($\{\breve{\cdot}\}$) over the interface C, e.g. $[\![\breve{W} \cdot \breve{N}]\!] = \breve{W}^+ \cdot \breve{N}^+ + \breve{W}^- \cdot \breve{N}^- = \breve{W}^+ - \breve{W}^- \cdot \breve{N}^+ = \breve{W} \cdot \breve{N}$ where the superscripts $^+$ and $^-$ denote the surface quantity on the outward and inward of the interface, respectively, and we define the surface outward normal vector $\breve{N} := \breve{N}^+$ over the interface C_k.

2.1 Key concepts of differential geometry

We briefly review the key concepts of differential geometry required to describe the kinematics of the bulk and surface. Further details on differential geometry can be found in books and papers, for example, Gurtin [25], Green [23], Steinmann [37, 54] and Do Carmo [19].

We first focus on the bulk description. Let r be an arbitrary vector expressed in terms of the individual components of the curvilinear coordinate system, i.e., $r = r(\xi^1, \xi^2, \xi^3)$. We can always associate two new triplets of vectors (a_i and a^i) with the general curvilinear coordinates ξ^i by [28]

$$a_i = \frac{\partial r}{\partial \xi^i} \quad \text{and} \quad a^i = \frac{\partial \xi^i}{\partial r} \tag{1a}$$

$$I = \delta^i_j \, a_i \otimes a^j \quad \text{where} \quad \delta^i_j = a^i \cdot a_j \tag{1b}$$

where a_i and a^i are referred to as covariant and contravariant basis vectors, respectively, and δ^i_j are the mixed-variant identity tensor and the mixed Kronecker delta, respectively. Note that $\delta^i_j = 1$ for $i = j$, and $\delta^i_j = 0$ for $i \neq j$ ($i, j = 1, 2, 3$).

The covariant and contravariant basis vectors are not necessarily orthogonal to each other but linearly independent, requiring $(a_1 \times a_2) \cdot a_3 \neq 0$ (the vectors do not lie in a plane) [29]. The vectors a_i and a^i are connected to metric tensors a_{ij}, a^{ij} by

$$a_i = a_{ij} a^j \quad \text{with} \quad a_{ij} = a_{ji} = a_i \cdot a_j \tag{2a}$$

$$a^i = a^{ij} a_j \quad \text{with} \quad a^{ij} = a^{ji} = a^i \cdot a^j \tag{2b}$$

where two tensors are inverse to each other, i.e., $a_{ik} a^{kj} = \delta^j_i$. Note that metric tensors with the identical indices represent the squares of the lengths; for example, $a_{11} = |a_1|^2$, whereas the metric tensors with different indices represent the products of the lengths and the cosine of the angle θ; for example, $a_{12} = |a_1||a_2| \cos(\theta(a_1, a_2))$.

If a quantity $\{\bullet\}$ is a vector field defined throughout volume V which is bounded by a closed surface S, then bulk $\{\bullet\}$ and $\{\breve{\bullet}\}$ gradient and divergence operators in 3D general curvilinear coordinates are defined as follows:

$$\nabla_X \{\bullet\} = \frac{\partial \{\bullet\}}{\partial \xi^i} \otimes a^i \tag{3a}$$

$$\nabla_X \cdot \{\bullet\} = \frac{\partial \{\bullet\}}{\partial \xi^i} \cdot a^i = \nabla_X \{\bullet\} : I \tag{3b}$$

With the above equations, the divergence theorem is [23]

$$\int_V \nabla_X \{\bullet\} \, dV = \int_S \{\bullet\} N \, dS \tag{4}$$

where N is a unit outward normal vector on the surface S.

We now move our attention to the surface description. Let $\breve{r}$ denote an arbitrary vector expressed in terms of the individual components of the general surface curvilinear coordinate system, i.e., $\breve{r} = \breve{r}(\xi^1, \xi^2)$. We can always associate two new doublets of vectors ($\breve{a}_\alpha$ and $\breve{a}^\alpha$) with the general curvilinear coordinates ξ^α by coordinate transformations [23].

$$\breve{a}_\alpha = \frac{\partial \breve{r}}{\partial \xi^\alpha} \quad \text{and} \quad \breve{a}^\alpha = \frac{\partial \xi^\alpha}{\partial \breve{r}} \tag{5a}$$

$$\breve{I} = \delta^\alpha_\beta \, \breve{a}_\alpha \otimes \breve{a}^\beta \quad \text{where} \quad \delta^\alpha_\beta = \breve{a}^\alpha \cdot \breve{a}_\beta \tag{5b}$$

where $\breve{a}_\alpha$ and $\breve{a}^\alpha$ are referred to as covariant and contravariant surface basis vectors, respectively, and δ^α_β are the mixed-variant surface identity tensor and the mixed Kronecker delta, respectively ($\alpha, \beta = 1, 2$). Note that the surface identity tensor also can be expressed by $\breve{I} = I - N \otimes N$.

The vectors $\breve{a}_\alpha$ and $\breve{a}^\alpha$ are connected with the geometrical characteristics

$$\breve{a}_\alpha = \breve{a}_{\alpha\beta} \breve{a}^\beta \quad \text{with} \quad \breve{a}_{\alpha\beta} = \breve{a}_{\beta\alpha} = \breve{a}_\alpha \cdot \breve{a}_\beta \tag{6a}$$

$$\mathbf{a}_\alpha = \mathbf{a}^\beta \mathbf{a}_{\alpha\beta} \quad \text{with} \quad \mathbf{a}^{\alpha\beta} = \mathbf{a}^{\beta\alpha} = \mathbf{a}^\alpha \cdot \mathbf{a}^\beta \tag{6b}$$

where $\mathbf{a}_{\alpha\beta}$ and $\mathbf{a}^{\alpha\beta}$ are surface metric tensors, and these two mappings are inverse to each other, i.e. $\mathbf{a}^{\alpha\gamma}\mathbf{a}_{\gamma\beta} = \boldsymbol{\delta}^\alpha_\beta$.

If a quantity $\{\bullet\}$ is a surface vector field defined throughout a surface S, which is bounded by a closed curve L, then the surface gradient and divergence operators in a 2D general curvilinear coordinates are defined as follows:

$$\nabla_{\mathbf{X}}\{\bullet\} = \frac{\partial\{\bullet\}}{\partial \xi^\alpha} \otimes \mathbf{a}^\alpha \tag{7a}$$

$$\nabla_{\mathbf{X}} \cdot \{\bullet\} = \frac{\partial\{\bullet\}}{\partial \xi^\alpha} \cdot \mathbf{a}^\alpha = \nabla_{\mathbf{X}}\{\bullet\} : \mathbf{I} \tag{7b}$$

With the above equations, we introduce the surface divergence theorem as follows [54]:

$$\int_S \nabla_{\mathbf{X}} \cdot \{\bullet\}\, \mathrm{dS} = \int_L \{\bullet\} \cdot \mathbf{N}\, \mathrm{dL} - \int_S \kappa \{\bullet\} \cdot \mathbf{N}\, \mathrm{dS} \tag{8}$$

where $\mathbf{N}$ is the unit outward bi-normal vector to the boundary curve L (see Fig. 1), and $\kappa = \nabla_{\mathbf{X}} \cdot \mathbf{N}$ is the total curvature (twice the mean surface curvature) [25].

2.2 Kinematics

We use the notation $\chi : \mathrm{V} \to \mathrm{R}^3$ for the deformation of body B. A motion χ is the vector field of the mapping $\mathbf{x} = \chi(\mathbf{X}, t)$ of a material point in the reference configuration $\mathbf{X} \in \mathrm{V}$ to a position in the deformed configuration $\mathbf{x} \in \mathrm{v}$. The kinematics of a typical particle are described by the displacement vector field in the spatial description, $\mathbf{u}(\mathbf{X}, t) = \mathbf{x}(\mathbf{X}, t) - \mathbf{X}$. The kinematics of an infinitesimal bulk element are described by

$$\mathbf{F}(\mathbf{X}, t) = \frac{\partial \chi(\mathbf{X}, t)}{\partial \mathbf{X}} = \nabla_{\mathbf{X}} \mathbf{x}(\mathbf{X}, t) \tag{9a}$$

$$\mathbf{F}^{-1}(\mathbf{x}, t) = \frac{\partial \chi^{-1}(\mathbf{x}, t)}{\partial \mathbf{x}} = \nabla_{\mathbf{x}} \mathbf{X}(\mathbf{x}, t) \tag{9b}$$

where $\mathbf{F}(\mathbf{X}, t)$ and $\mathbf{F}^{-1}(\mathbf{x}, t)$ are the deformation gradient and inverse deformation gradient, respectively. Note that $J(\mathbf{X}, t) = dv/dV = \det \mathbf{F}(\mathbf{X}, t) > 0$ is the Jacobian determinant of the deformation gradient defining the ratio of a volume element between the material and spatial configuration.

Assuming conformity, the surface displacement $\hat{\mathbf{u}}(\mathbf{X}, t) = \hat{\mathbf{x}}(\mathbf{X}, t) - \mathbf{X}$ can be determined by $\mathbf{u}_S(\mathbf{X}, t) = \mathbf{u}(\mathbf{X}, t)$. The motion of an arbitrary differential vector element $d\mathbf{X}$ can be mapped by the deformation gradient $\mathbf{F}$ to a vector $d\mathbf{x}$ in the deformed configuration. However, a unit normal vector $\mathbf{N}$ in the material configuration cannot be transformed into a unit normal vector $\mathbf{n}$ in the spatial configuration using solely the deformation gradient [29, 54]. This motivates us to follow the kinematics of an infinitesimal surface element [38, 39].

$$\hat{\mathbf{F}}(\mathbf{X}, t) = \frac{\partial \hat{\chi}(\mathbf{X}, t)}{\partial \mathbf{X}} \cdot \hat{\mathbf{I}} = \nabla_{\mathbf{X}} \hat{\mathbf{x}}(\mathbf{X}, t) \tag{10a}$$

$$\hat{\mathbf{F}}^{-1}(\hat{\mathbf{x}}, t) = \frac{\partial \chi^{-1}(\hat{\mathbf{x}}, t)}{\partial \hat{\mathbf{x}}} \cdot \hat{\mathbf{i}} = \nabla_{\hat{\mathbf{x}}} \mathbf{X}(\hat{\mathbf{x}}, t) \tag{10b}$$

where $\hat{\mathbf{F}}(\mathbf{X}, t)$ and $\hat{\mathbf{F}}^{-1}(\hat{\mathbf{x}}, t)$ are the surface deformation gradient and inverse surface deformation gradient tensors. Note mapping from the bulk (3D) to the surface (2D), so it is rank deficient (it has rank 2, whereas full-rank would be 3). The $\hat{\mathbf{I}} = \mathbf{I} - \mathbf{N} \otimes \mathbf{N}$ and $\hat{\mathbf{i}} = \mathbf{i} - \mathbf{n} \otimes \mathbf{n}$ are the mixed surface unit tensors with the outward unit normal vectors $\mathbf{N}$ and $\mathbf{n}$, where $\hat{\mathbf{I}}$ and $\hat{\mathbf{i}}$ act as a surface (idempotent) projection tensor in material and spatial configurations, respectively. Note that $J(\mathbf{X}, t) = da/dA = \det \hat{\mathbf{F}}(\mathbf{X}, t) > 0$ is the Jacobian determinant of the surface deformation gradient defining the area ratio of a surface element between material and spatial configuration.

We introduce $\mathbf{C} = \mathbf{F}^{\mathrm{T}}\mathbf{F}$ and $\hat{\mathbf{C}} = \hat{\mathbf{F}}^{\mathrm{T}}\hat{\mathbf{F}}$ the right Cauchy-Green tensors in the bulk and on the surface, respectively, as

$$\mathbf{C} = \mathbf{F}^{\mathrm{T}}\mathbf{F} \tag{11a}$$

$$\hat{\mathbf{C}} = \hat{\mathbf{F}}^{\mathrm{T}}\hat{\mathbf{F}} \tag{11b}$$

and $I_1 = \mathrm{tr}(\mathbf{C})$ is the first principal invariant. The detailed derivation for the surface kinematics can be found in Do Carmo [19], Green and Zerna [23], Steinmann [54]. Note that we cannot perform the inverse of the surface right Cauchy-Green tensor due to its rank deficiency. Nevertheless, we still obtain its inverse form in the generalized sense,

$$\hat{\mathbf{C}}^{-1} = \hat{\mathbf{I}}\mathbf{C}^{-1}\hat{\mathbf{I}} \tag{12}$$

which will be utilized in the forthcoming developments for defining the surface kinetic law.

2.3 Mechanical equilibrium

Mechanical equilibrium is assumed to be maintained at all times during the motion. The strong form of the corresponding governing equation is

$$\nabla_{\mathbf{X}} \cdot \mathbf{P} + \mathbf{B} = 0 \quad \text{in } \mathrm{V} \tag{13a}$$

$$\mathbf{P}\mathbf{N} - \nabla_{\mathbf{X}} \cdot \hat{\mathbf{P}} = \mathbf{T} \quad \text{on } S_T \tag{13b}$$

$$\mathbf{u} = \mathbf{u}_p \quad \text{on } S_u \tag{13c}$$

$$[\![\mathbf{P}\mathbf{N}]\!] = 0 \quad \text{on L} \tag{13d}$$

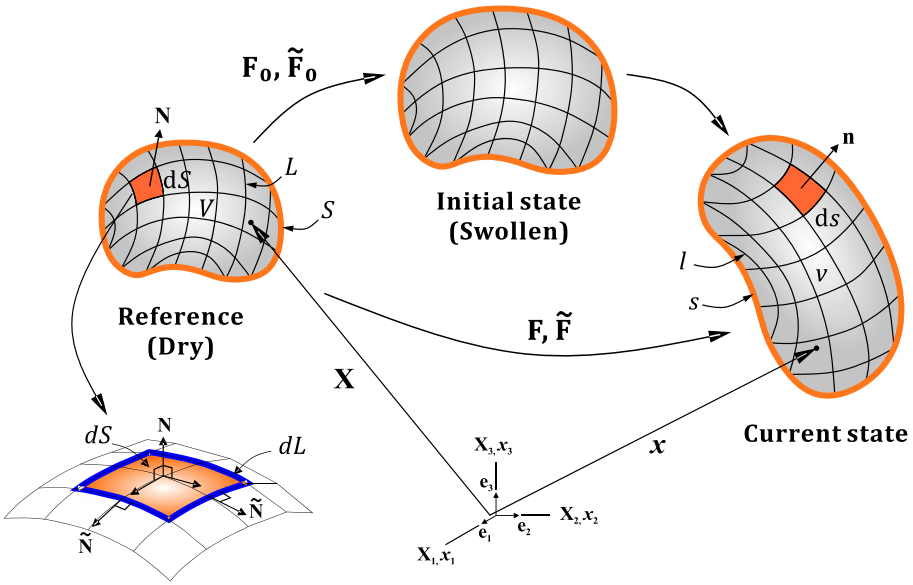

Fig. 1 Schematic illustration of the reference, initial, and current state of a continuum body. The initial state is assumed to be isotropically scaled from the reference state. The reference volume and surface, and boundary are denoted by V and S, and L respectively. The normal vector to the surface in the reference and current conguration (N and n) and the bi-normal vector to the boundary ($\tilde{N}$) are shown, where the over-tilde indicates surface quantities

where P and $\tilde{P}$ are the rst Piola-Kirchoff stresses in bulk and on surface, B and T are the body force and the traction vector, and μ_p is the prescribed displacement. Note that a Neumann-type boundary condition is also ned on boundary curves that [[•]] indicates summation over surfaces intersecting on boundary curves [54].

2.4 Species balance

Through species (or mass) balance, the strong form for the corresponding governing equation is [50]:

$$\dot{C} + \nabla_X \cdot J = r \quad \text{in } V \tag{14a}$$

$$\dot{\tilde{C}} + \tilde{\nabla}_X \cdot \tilde{J} - J \cdot N = i \quad \text{on } S_{\tilde{c}} \tag{14b}$$

$$\tilde{J} = \tilde{J}_p \quad \text{on } S_{\tilde{j}} \tag{14c}$$

$$[[\tilde{J} \cdot \tilde{N}]] = 0 \quad \text{on } L \tag{14d}$$

where C is the bulk nominal concentration (the number of species per unit reference volume), $\tilde{C}$ is the surface nominal concentration (the number of species per unit reference area), J is the bulk nominal ux (the number of species per unit time per unit area), and $\tilde{J}$ is the surface nominal ux (the number of species per unit time per unit length). The r and i are the source/sink terms for the number of species injected into the reference volume and area per unit time, and $\tilde{J}_p$ is the prescribed surface ux. Equation (14a) is the standard species balance equation prescribed for the bulk in the reference conguration. Equation (14b) describes the species balance on the surface, where the third term on the left-hand is similar to the source i , but describes the outward normal ux from the bulk to the surface; note that species can get to the surface either from the exterior (environment) or from the interior (bulk). Additionally, Eq. (14) are supplemented with initial conditions,

$$C(X, t = 0) = C_0 \tag{15a}$$

$$\tilde{C}(\tilde{X}, t = 0) = \tilde{C}_0 \tag{15b}$$

where C_0 and $\tilde{C}_0$ are the initial species concentration in the bulk and on the surface at time $t = 0$. Note that we assume homogeneous initial conditions; this choice will become apparent as we discuss the general solution process for the corresponding boundary value problems in Sect. 5.

2.5 Thermodynamic considerations

In addition to the free energy density in the bulk, we consi the free energy density on the surface. We will denote the and surface free energy densities as

$$\hat{A}(F, C) \quad \text{and} \quad \tilde{\hat{A}}(\tilde{F}, \tilde{C}) \tag{16}$$

where we assume that they are functions of the deformati gradient and nominal concentration in the bulk and on the surface, respectively.

Considering a system that includes an elastic and porou solid component coupled with species that are free to mig in the porous network, the rate of change of the system's energy G has to account for several effects [2, 13, 27, 29, This can be expressed as

$$\dot{G} = \int_V \dot{\hat{A}}\, dV + \int_{S_{\tilde{A}}} \dot{\tilde{\hat{A}}}\, dS - \int_V B\dot{x}\, dV - \int_S T\dot{x}\, dS - \int_V \mu r\, dV - \int_{S_{\tilde{A}}} \tilde{\mu} i\, dS \tag{17}$$

where the third and fourth terms are the rate of mechanical work by the body force B and traction vector T, and the fifth and sixth terms are the rate of chemical work by the bulk chemical potential μ and the surface chemical potential $\hat{\mu}$. Note that thermodynamics dictate that the free energy of the system should not increase, i.e. $\dot{G} \leq 0$,

Substituting Eqs. (13) and (14) into Eq. (17), the rate of change of the free energy of the system can be expressed as follows,

$$\begin{aligned}\dot{G} = &\int_V \dot{\tilde{A}}\, dV + \int_S \dot{\hat{\tilde{A}}}\, dS - \int_V \mathbf{P} : \dot{\mathbf{F}}\, dV \\ &- \int_S \hat{\mathbf{P}} : \dot{\hat{\mathbf{F}}}\, dS \\ &- \int_V \mu \dot{C}\, dV - \int_S \hat{\mu} \dot{\hat{C}}\, dS \\ &+ \int_S (\hat{\mu} - \mu \mathbf{J}) \cdot \mathbf{N}\, dS \\ &+ \int_V \mathbf{J} \cdot \nabla_X \mu\, dV \\ &+ \int_S \hat{\mathbf{J}} \cdot \nabla_{\hat{X}} \hat{\mu}\, dS \leq 0 \end{aligned} \tag{18}$$

Using the chain-rule, the rate of bulk and surface free energy densities can be expressed as

$$\dot{\tilde{A}} = \frac{\partial \tilde{A}}{\partial \mathbf{F}} : \dot{\mathbf{F}} + \frac{\partial \tilde{A}}{\partial C} \dot{C} \tag{19a}$$

$$\dot{\hat{\tilde{A}}} = \frac{\partial \hat{\tilde{A}}}{\partial \hat{\mathbf{F}}} : \dot{\hat{\mathbf{F}}} + \frac{\partial \hat{\tilde{A}}}{\partial \hat{C}} \dot{\hat{C}} \tag{19b}$$

By substituting Eq. (19) into Eq. (18), and rearranging terms yields

$$\begin{aligned}\dot{G} = &\int_V \left(\frac{\partial \tilde{A}}{\partial \mathbf{F}} - \mathbf{P} \right) : \dot{\mathbf{F}}\, dV \\ &+ \int_S \left(\frac{\partial \hat{\tilde{A}}}{\partial \hat{\mathbf{F}}} - \hat{\mathbf{P}} \right) : \dot{\hat{\mathbf{F}}}\, dS \\ &+ \int_V \left(\frac{\partial \tilde{A}}{\partial C} - \mu \right) \dot{C}\, dV \\ &+ \int_S \left(\frac{\partial \hat{\tilde{A}}}{\partial \hat{C}} - \hat{\mu} \right) \dot{\hat{C}}\, dS \\ &+ \int_S (\hat{\mu} - \mu \mathbf{J}) \cdot \mathbf{N}\, dS + \int_V \mathbf{J} \cdot \nabla_X \mu\, dV \\ &+ \int_S \hat{\mathbf{J}} \cdot \nabla_{\hat{X}} \hat{\mu}\, dS \leq 0 \end{aligned} \tag{20}$$

where each integral represents a distinct mechanism of energy dissipation, associated with mechanical and chemical works. The inequality must hold at every point of the continuum body and at all times during a thermodynamical process. To satisfy the constraint, the Coleman-Noll procedure [29] states that each integrand in Eq. (20) to be either negative or equal to zero.

For the first four terms in Eq. (20) we obtain the following constitutive relations

$$\mathbf{P} = \frac{\partial \tilde{A}(\mathbf{F}, C)}{\partial \mathbf{F}} \quad \text{and} \quad \mu = \frac{\partial \tilde{A}(\mathbf{F}, C)}{\partial C} \tag{21a}$$

$$\hat{\mathbf{P}} = \frac{\partial \hat{\tilde{A}}(\hat{\mathbf{F}}, \hat{C})}{\partial \hat{\mathbf{F}}} \quad \text{and} \quad \hat{\mu} = \frac{\partial \hat{\tilde{A}}(\hat{\mathbf{F}}, \hat{C})}{\partial \hat{C}} \tag{21b}$$

for the bulk and surface first Piola–Kirchhoff stresses tensors and the bulk and surface chemical potentials, respectively.

For the fifth term in Eq. (20), the most obvious way to guarantee the dissipation inequality on surface is to impose the condition [50],

$$\mu(X, t) = \hat{\mu}(\hat{X}, t) \text{ on } S \tag{22}$$

which prescribes local chemical equilibrium between the surface and the bulk. This point is discussed in McBride et al [50], where also the possibility of an alternate strategy to satisfy that constraint is highlighted.

Finally, to maintain that the last two terms in Eq. (20) remain to be negative or zero, we adopt kinetic laws for diffusion [31] in bulk and on surface. This allows us to maintain negative semi-definiteness and describes the constituent species diffusion that is driven by gradients of chemical potential:

$$\mathbf{J} = -\mathbf{M} \nabla_X \mu \tag{23a}$$

$$\hat{\mathbf{J}} = -\hat{\mathbf{M}} \nabla_{\hat{X}} \hat{\mu} \tag{23b}$$

where $\mathbf{M}$ and $\hat{\mathbf{M}}$ are the bulk and surface mobility tensors. In the upcoming section, we will specialize the symmetric and positive definite mobility tensors $\mathbf{M}$ and $\hat{\mathbf{M}}$ to fully define the constitutive laws for the fluxes.

3 Specific considerations for hydrogels

In this work, we will focus on a coupled bulk and surface poroelastic framework for hydrogels. We have to specialize our choices for the surface and bulk free energy densities, the corresponding constitutive laws, and definition of mobility tensors for our theory to be complete and to be able to proceed to the development of the numerical solution scheme.

3.1 Particularizing the surface and bulk free energy densities

For the free energy densities of polymer in the bulk, we adopt the Flory-Huggins model [22, 31, 57], assuming

the following additive decomposition into elastic and mixing contributions

$$\tilde{A}(F, C) = \tilde{A}_e(F) + \tilde{A}_m(C). \quad (24)$$

These can be individually specialized to

$$\tilde{A}_e(F) = \frac{1}{2} N k_B T (I_1 - 3 - 2 \ln J) \quad (25a)$$

$$\tilde{A}_m(C) = -\frac{k_B T}{\Omega} \left[\Omega C \ln \frac{1 + \Omega C}{\Omega C} + \frac{\chi}{1 + \Omega C} \right] \quad (25b)$$

where Ω is the volume of a solvent molecule, χ is a dimensionless parameter of polymer-solvent mixing, N is the number of polymer chains per reference volume, k_B is Boltzmann's constant, and T is the absolute temperature. Note that the first and second terms in (25b) represent the entropy and enthalpy of mixing, respectively [31].

Following [2, 12, 13, 31, 32], we assume that the polymer chains and the diffusion species are individually incompressible. Furthermore, the gel is a condensed matter with negligible void space, so any volume change of the hydrogel is due to species diffusion, thus

$$1 + \Omega C = J \Rightarrow C = \frac{J - 1}{\Omega}. \quad (26)$$

Similar to Eq. (24), we assume that the surface free energy density of the hydrogel is also decomposed into elastic and mixing contributions as (see Remark 2))

$$\hat{A}(\hat{F}, \hat{C}) = \hat{A}_e(\hat{F}, \hat{C}) + \beta \hat{A}_m(\hat{C}) \quad (27)$$

which can be individually expressed as

$$\hat{A}_e(\hat{F}, \hat{C}) = \frac{\hat{\kappa}}{2} \left(J^{\hat{\Omega}} - 1 - \hat{\Omega} \hat{C} \right)^2 + \hat{\gamma} J^{\hat{\Omega}} \quad (28a)$$

$$\hat{A}_m(\hat{C}) = -\frac{k_B T}{\hat{\Omega}} \left[\hat{\Omega} \hat{C} \ln \frac{1 + \hat{\Omega} \hat{C}}{\hat{\Omega} \hat{C}} + \frac{\hat{\chi}}{1 + \hat{\Omega} \hat{C}} \right] \quad (28b)$$

In a microscopic description, the length scales of polymer chains and solvent molecules are very different. Focusing on the surface, where the interaction of polymer chains and solvent molecules is crucial, and more specifically the finite thickness of the surface zone, here we consider the the realization of a constant number of β layer potential sites that solvent molecules can occupy in the surface zone. Here, $\hat{\Omega}$ is the area that a solvent molecule occupies on the surface, $\hat{\chi}$ is a dimensionless parameter of polymer-solvent mixing. In the second term of the right hand side of Eq. (28a), we consider a constant surface energy per unit current area $\hat{\gamma}$ [J/m^2], which leads to a fluid-like response for the surface gate. Additionally, it is not realistic to enforce the equivalent of incompressibility for the surface, as one cannot constrain the number of layers of species on the surface, even though the constituents are individually incompressible. Thus, we introduce a penalty term to loosely introduce a constraint for species concentration in the surface connected to the area change of the boundary, with a penalty coefficient $\hat{\kappa}$ [J/mol/m^2].

Remark 2 (The application of Flory-Huggins model to surface poroelasticity) In the Flory-Huggins model [22, 33], the solvent and polymer molecules are considered to be arranged in the 3D lattice sites such that each site may be occupied either by a solvent molecule or by a segment of the polymer chain, and the equations of entropy and enthalpy of mixing are derived in the statistical thermodynamics approach (see Chapter 7 of [57] for the details). Without loss of generality, the Flory-Huggins model can be also considered on the 2D lattice model, where the probability of encountering a site occupied by the solvent and polymer molecules is the fraction of the area. Although the number of adjacent sites would be different in 2D and 3D models, the Flory parameters χ and $\hat{\chi}$ are introduced to eliminate the number of adjacent sites, and their dependence on the dimensionality is to be fitted to experimental data. We introduce the parameter β in the mixing part of surface free energy to account for the number of 2D lattice layers that arise due to the size difference of solvent molecules and polymer chains considering the surface zone, but we do not consider the interaction energy between the layers. Note that the elastic part of surface free energy $\hat{A}_e$ does not include the number of layer parameter β and we assume to be a constant.

3.2 Constitutive relations

Using Equation (21), (25) and (28), the specific constitutive relations are obtained as follows:

$$P = N k_B T \left[F + \alpha_1 J F^{-T} \right] \text{ with}$$

$$\alpha_1 = -\frac{1}{J} + \frac{1}{N\Omega} \left[\frac{1}{J} + \ln \frac{J - 1}{J} + \frac{\chi}{J^2} \right] \quad (29a)$$

$$\mu = k_B T \left[\ln \frac{\Omega C}{1 + \Omega C} + \frac{1}{1 + \Omega C} + \frac{\chi}{(1 + \Omega C)^2} \right] \quad (29b)$$

$$\hat{P} = \hat{\kappa} \left(J^{\hat{\Omega}} - 1 - \hat{\Omega} \hat{C} \right) J^{\hat{\Omega}} F^{-T} + \hat{\gamma} J^{\hat{\Omega}} F^{-T} \quad (29c)$$

$$\hat{\mu} = k_B T \left[\ln \frac{\hat{\Omega} \hat{C}}{1 + \hat{\Omega} \hat{C}} + \frac{1}{1 + \hat{\Omega} \hat{C}} + \frac{\hat{\chi}}{(1 + \hat{\Omega} \hat{C})^2} \right] - \hat{\kappa} \hat{\Omega} \left(J^{\hat{\Omega}} - 1 - \hat{\Omega} \hat{C} \right) \Rightarrow \hat{C} = \hat{C}(\hat{\mu}, J) \quad (29d)$$

which are the specific forms of the constitutive relations for the first Piola–Kirchhoff stresses and the chemical potential in bulk and on the surface. Note that we do not use the

constitutive relation of Eq. (29b), but the incompressibility condition of Eq. (26) to determine the bulk concentration C. On the other hand, we do not have an incompressibility condition for solvent molecules on surface, and we should use the constitutive relation (29d) to determine the surface concentration $\breve{C}$. However, there is no closed-form solution for the surface concentration in Eq. (29d), so we need to solve the constitutive relation numerically.

3.3 Bulk and surface diffusion

Particularizing the expression for the bulk mobility, and following [31], and prescribing an equivalent definition for surface mobility

$$\mathbf{M} = \frac{\mathbf{C}\,\mathbf{D}}{k_B T}\mathbf{C}^{-1} \tag{30a}$$

$$\breve{\mathbf{M}} = \frac{\breve{\mathbf{C}}\,\breve{\mathbf{D}}}{k_B T}\breve{\mathbf{C}}^{-1} \tag{30b}$$

where k_B is the Boltzmann's constant, T is an absolute temperature. The coefficient of diffusion of the solvent molecules $\mathbf{D}$ in the bulk and $\breve{\mathbf{D}}$ on the surface are assumed to be isotropic and independent of the deformation and concentration as the simplest approximation [31]. Note that the current concentrations are related to the nominal concentrations as $c = C/J$ and $\breve{c} = \breve{C}/\breve{J}$. It is important to note that Eqs. (30a) and (30b) are formulated to consider the change of the porosity of the solid due to the finite deformations, as the mobility tensors are inversely proportional to the Green deformation tensors.

4 Mixed finite element formulation

This section presents a finite element formulation based on the nonlinear theory in Sects. 2 and 3. The main aim here is to provide an accessible open-source implementation that will be utilized by the research community, and thus, we choose FEniCS [1, 46] for the implementation; a choice which also affects the set-up of the mixed finite element formulation. The formulation starts with the strong form of the governing equations and initial and boundary conditions. We first introduce the weak form of the problem and subsequently describe the normalization, discretization, solution steps, and some specific implementation details for FEniCS. As the main focus here is the coupled mechanics between diffusion and deformation in bulk and on surface, we here-on neglect the source terms, i.e., $r = 0$.

4.1 Three-field weak form

Since the chemical boundary conditions for hydrogels are often specified in terms of chemical potential or diffusion flux (proportional to the gradient of chemical potential), it is convenient to use the chemical potential (instead of solvent concentration) as an independent variable in the finite element formulation. Additionally, this allows us to avoid C^1 continuity requirements [13]. For this purpose, we rewrite the free energy densities as a function of the deformation gradient and the chemical potential through a Legendre transform [31,50], which replaces a variable with its thermodynamic conjugate:

$$\psi_A(\mathbf{F}, \mu) = \tilde{\psi}_A(\mathbf{F}, C) - \mu C \tag{31a}$$

$$\breve{\psi}_A(\breve{\mathbf{F}}, \breve{\mu}) = \breve{\tilde{\psi}}_A(\breve{\mathbf{F}}, \breve{C}) - \breve{\mu}\breve{C} \tag{31b}$$

After the Legendre transform, similar to Equation (21), the constitutive relations can be rewritten as follows:

$$\mathbf{P} = \frac{\partial \psi_A(\mathbf{F}, \mu)}{\partial \mathbf{F}} \quad \text{and} \quad C = -\frac{\partial \psi_A(\mathbf{F}, \mu)}{\partial \mu} \tag{32a}$$

$$\breve{\mathbf{P}} = \frac{\partial \breve{\psi}_A(\breve{\mathbf{F}}, \breve{\mu})}{\partial \breve{\mathbf{F}}} \quad \text{and} \quad \breve{C} = -\frac{\partial \breve{\psi}_A(\breve{\mathbf{F}}, \breve{\mu})}{\partial \breve{\mu}} \tag{32b}$$

which yields the same constitutive relation for the surface Piola–Kirchhoff, but the bulk first Piola–Kirchhoff stress $\mathbf{P}$ should be modified because the incompressibility condition was enforced by substituting the Eq. (26) into Eq. (25) to eliminate the bulk concentration C [32]:

$$\mathbf{P} = N k_B T \left[\tilde{\mathbf{F}} + \alpha_2 J\, \tilde{\mathbf{F}}^{-T} \right] \quad \text{with}$$
$$\alpha_2 = -\frac{1}{J} + \frac{\beta}{N} \left[\frac{1}{J} + \ln\left(\frac{J-1}{J} \right) + \frac{\chi}{J^2} - \frac{\mu}{k_B T} \right] \tag{33}$$

Note that the bulk concentration C can still be obtained by incompressibility condition of Eq. (26), but the surface concentration is now given implicitly by solving a nonlinear algebraic equation in Eq. (29d).

Keeping into account the inability of the FEniCS framework to solve nonlinear equations at the Gauss-point level, we proceed to solve Eq. (29d) directly with the mixed finite element method. The weak form of the problem is obtained by using a set of test functions, which satisfy the necessary integrability conditions. By multiplying Eqs. (13a), (14a) and (29d) with the test functions δu, $\delta\mu$, and $\delta\breve{\mu}$, and integrating over the domains Ω and Γ, respectively, then we obtain that

$$\int_V \mathbf{P} : \nabla_X \delta u \, dV + \int_S \breve{\mathbf{P}} : \breve{\nabla}_X \delta u \, dS = 0 \tag{34a}$$

$$\int_V \dot{C}\, \delta\mu \, dV - \int_V \mathbf{J} \cdot \nabla_X \delta\mu \, dV + \int_S \dot{\breve{C}}\, \delta\mu \, dS - \int_S \breve{\mathbf{J}} \cdot \breve{\nabla}_X \delta\mu \, dS = 0 \tag{34b}$$

$$\int_S \left[\tilde{\mu} - k_B T \left(\ln\frac{\tilde{c}}{1+\tilde{c}} + \frac{1}{1+\tilde{c}} + \frac{\chi}{(1+\tilde{c})^2}\right)\right]\delta\tilde{c}\, dS - \tilde{\kappa}\int_S \left(\frac{1}{\tilde{c}} - 1\right)\delta\tilde{c}\, dS = 0 \tag{34c}$$

where the derivation of Eq. (34b) can be found in Appendix A. The statement of the weak form is to find the trial functions, μ, μ and c, such that the integrals in Eq. (34) are satisfied for any permissible test functions, δc, $\delta\mu$ and $\delta\mu$.

4.2 Normalization

For the finite element simulations in the following section, all variables and parameters are normalized, as denoted by $\{\tilde{\bullet}\}$. All lengths are normalized by a characteristic dimension, H (e.g. the length of the edge of a cube in the reference configuration). The chemical potential and stresses are normalized as follows,

$$\tilde{\mu} = \frac{\mu}{k_B T}, \quad \tilde{P} = \frac{P}{N k_B T}, \quad \tilde{\mathbf{P}} = \frac{\mathbf{P}}{N k_B T H} \tag{35}$$

Following the normalization of the surface stress, surface energy and penalty coefficient should be normalized in the same way,

$$\tilde{\gamma} = \frac{\gamma}{N k_B T H}, \quad \tilde{\kappa} = \frac{\kappa}{N k_B T H} \tag{36}$$

Solvent concentration and time are normalized as follows,

$$\tilde{c} = Cc, \qquad \tilde{\mathbf{x}} = \frac{\mathbf{x}}{H}, \qquad \hat{t} = \frac{t}{\tau} \tag{37}$$

where $\tau = H^2/D$ is the characteristic time scale of diffusion.

Recall that the shear modulus linearized about the undeformed dry state ($\mathbf{F} = \mathbf{I}$) is $G = Nk_BT$ [12]. In a homogeneously swollen stress-free state, the deformation gradient takes the form $\mathbf{F} = \lambda_0 \mathbf{I}$, with λ_0 the swelling stretch, the shear modulus about that state is defined as follows [12],

$$G_0 = \frac{N k_B T}{\lambda_0} \tag{38}$$

Considering again a homogeneously swollen state, the elastocapillary length scale is defined by $\ell_0 = \gamma_0/G_0$ for constant surface free energy per unit current surface area. Taking into account the characteristic dimension H the normalized elastocapillary length scale is given as

$$\tilde{\ell} = \frac{\ell_0}{H} = \tilde{\gamma}_0 \lambda_0 \tag{39}$$

By substituting the normalized variables into the weak forms in Equation (34), we can obtain the normalized weak forms,

for the bulk and the surface.

$$\int_V \tilde{\mathbf{P}} : \nabla_{\tilde{\mathbf{x}}}\delta\tilde{\mu}\, dV + \int_S \tilde{\mathbf{P}} : \nabla_{\tilde{\mathbf{x}}}\delta\tilde{\mu}\, dS = 0 \tag{40a}$$

$$\frac{\partial H}{\partial t}\int_V \frac{dc}{dt}\delta\tilde{\mu}\, dV - \int_V \mathbf{J}\cdot\nabla_{\tilde{\mathbf{x}}}\delta\tilde{\mu}\, dV + \int_S \frac{dc}{dt}\delta\tilde{\mu}\, dS - \int_S \mathbf{J}\cdot\nabla_{\tilde{\mathbf{x}}}\delta\tilde{\mu}\, dS = 0 \tag{40b}$$

$$\int_S \left[\tilde{\mu} - \ln\frac{\tilde{c}}{1+\tilde{c}} - \frac{1}{1+\tilde{c}} - \frac{\chi}{(1+\tilde{c})^2}\right]\delta\tilde{c}\, dS + N\tilde{\ell}^2\int_S \left(\frac{1}{\tilde{c}} - 1\right)\delta\tilde{c}\, dS = 0 \tag{40c}$$

where N and $N\tilde{\ell}^2$ are the dimensionless parameters, and the normalized fluxes in bulk and on surface are obtained

$$\mathbf{J} = -\tilde{c}\mathbf{C}^{-1}\cdot\nabla_{\tilde{\mathbf{x}}}\tilde{\mu} \tag{41a}$$

$$\mathbf{J}_s = -\tilde{c}\frac{D_s}{D}\mathbf{C}^{-1}\cdot\nabla_{\tilde{\mathbf{x}}}\tilde{\mu} \tag{41b}$$

where D_s/D is the ratio of diffusivity between in bulk and on surface.

4.3 Temporal discretization

The backward Euler scheme is used to integrate Eq. (40b) over time:

$$\frac{\partial H}{\partial t}\int_V \frac{1}{\Delta\hat{t}}\left(\tilde{c}^{\hat{t}+\Delta\hat{t}} - \tilde{c}^{\hat{t}}\right)\delta\tilde{\mu} - \int_V \mathbf{J}^{\hat{t}+\Delta\hat{t}}\cdot\nabla_{\tilde{\mathbf{x}}}\delta\tilde{\mu}\, dV + \int_S \frac{1}{\Delta\hat{t}}\left(\tilde{c}^{\hat{t}+\Delta\hat{t}} - \tilde{c}^{\hat{t}}\right)\delta\tilde{\mu} - \int_S \mathbf{J}_s^{\hat{t}+\Delta\hat{t}}\cdot\nabla_{\tilde{\mathbf{x}}}\delta\tilde{\mu}\, dS = 0 \tag{42}$$

where the superscripts indicate the time step, at the current time step ($\hat{t} + \Delta\hat{t}$) or the previous step. We can combine Eqs. (40a), (40c) and (42) as

$$\begin{aligned}
&\int_V \tilde{\mathbf{P}} : \nabla_{\tilde{\mathbf{x}}}\delta\tilde{\mu}\, dV + \int_S \tilde{\mathbf{P}} : \nabla_{\tilde{\mathbf{x}}}\delta\tilde{\mu}\, dS \\
&+ \frac{\partial H}{\partial t}\int_V \frac{1}{\Delta\hat{t}}\left(\tilde{c}^{\hat{t}+\Delta\hat{t}} - \tilde{c}^{\hat{t}}\right)\delta\tilde{\mu} - \mathbf{J}^{\hat{t}+\Delta\hat{t}}\cdot\nabla_{\tilde{\mathbf{x}}}\delta\tilde{\mu}\, dV \\
&+ \int_S \frac{1}{\Delta\hat{t}}\left(\tilde{c}^{\hat{t}+\Delta\hat{t}} - \tilde{c}^{\hat{t}}\right)\delta\tilde{\mu} - \mathbf{J}_s^{\hat{t}+\Delta\hat{t}}\cdot\nabla_{\tilde{\mathbf{x}}}\delta\tilde{\mu}\, dS \\
&+ \int_S \left[\tilde{\mu} - \ln\frac{\tilde{c}}{1+\tilde{c}} - \frac{1}{1+\tilde{c}} - \frac{\chi}{(1+\tilde{c})^2}\right]\delta\tilde{c}\, dS \\
&+ N\tilde{\ell}^2\int_S \left(\frac{1}{\tilde{c}} - 1\right)\delta\tilde{c}\, dS = 0
\end{aligned} \tag{43}$$

where the superscript $(\cdot)^{n+1}$ is omitted for all the terms at the current time step and $(\cdot)^{n}$ are the species concentration at the previous time step in the bulk and on the surface.

4.4 Spatial discretization

A mixed finite element method is utilized to solve for the normalized displacement, chemical potential and surface concentration fields concurrently. To avoid the numerical instability with the mixed method, we should employ proper spatial discretization techniques [13]. We utilize a Taylor–Hood element [56] for the bulk quantities (displacement and chemical potential), where the interpolation order for chemical potential (linear) is one-order lower than for the displacement (quadratic). We note that a linear interpolation is utilized for the surface concentration field.

The normalized displacement and chemical potential are interpolated through the domain of interest as

$$\check{u} = \check{H}^{u}\check{d}^{u}, \qquad \check{\mu} = \check{H}^{\mu}\check{d}^{\mu}, \qquad \hat{c} = \hat{H}^{c}\hat{d}^{c} \tag{44}$$

where $\check{H}^{u}$, $\check{H}^{\mu}$ and $\hat{H}^{c}$ are the shape functions, and $\check{d}^{u}$, $\check{d}^{\mu}$ and $\hat{d}^{c}$ are the nodal values of the normalized displacement, chemical potential and surface concentration, respectively. Note that the shape function $\hat{H}^{c}$ is only defined on surface elements. The test functions are discretized in the same way

$$\delta\check{u} = \check{H}^{u}\delta\check{d}^{u}, \quad \delta\check{\mu} = \check{H}^{\mu}\delta\check{d}^{\mu}, \quad \delta\hat{c} = \hat{H}^{c}\delta\hat{d}^{c} \tag{45}$$

The stresses, concentrations and fluxes are evaluated at integration points, depending on the gradients of the displacement and chemical potential via the constitutive relations. Taking the gradient of Eq. (44), we obtain that

$$\nabla_{\check{X}}\check{u} = \nabla_{\check{X}}\check{H}^{u}\check{d}^{u} = \check{B}^{u}\check{d}^{u} \tag{46a}$$

$$\nabla_{\check{X}}\check{\mu} = \nabla_{\check{X}}\check{H}^{\mu}\check{d}^{\mu} = \check{B}^{\mu}\check{d}^{\mu} \tag{46b}$$

$$\nabla_{\hat{X}}\hat{c} = \nabla_{\hat{X}}\hat{H}^{c}\hat{d}^{c} = \hat{B}^{c}\hat{d}^{c} \tag{46c}$$

where $\check{B}^{u}$ and $\check{B}^{\mu}$ are the gradients of the shape functions in the bulk, and $\hat{B}^{c}$ is the one on the surface.

4.5 Nonlinear solution

The weak form in Eq. (43) can be expressed as a system of nonlinear equations,

$$\mathrm{N}(\mathrm{d}) = \mathrm{f} \quad \text{with} \quad \mathrm{d} = \begin{bmatrix} \check{d}^{u} & \check{d}^{\mu} & \hat{d}^{c} \end{bmatrix}^{\mathrm{T}} \tag{47}$$

Note that $\mathrm{N}(\mathrm{d})$ denotes the part of the weak form that is not known at current time step, we take all the known quantities to the right-hand side and denote as f (which is known from previous time step). The residual of nonlinear equations in iteration step is given by $\mathrm{R} = \mathrm{f} - \mathrm{N}(\mathrm{d})$, which can be solved using the Newton–Raphson method. In particular, the procedure requires the calculation of the tangent Jacobian matrix at each iteration, namely,

$$\frac{\partial \mathrm{N}^{\mathrm{I}}}{\partial \mathrm{d}^{\mathrm{J}}} = \begin{bmatrix} \mathrm{K}^{\check{u}\check{u}} & \mathrm{K}^{\check{u}\check{\mu}} & \mathrm{K}^{\check{u}\hat{c}} \\ \mathrm{K}^{\check{\mu}\check{u}} & \mathrm{K}^{\check{\mu}\check{\mu}} & \mathrm{K}^{\check{\mu}\hat{c}} \\ \mathrm{K}^{\hat{c}\check{u}} & \mathrm{K}^{\hat{c}\check{\mu}} & \mathrm{K}^{\hat{c}\hat{c}} \end{bmatrix} \tag{48}$$

FEniCS version 2019.2.0 [6] is used to numerically solve the coupled non-linear equations via the Portable Extensible Toolkit for Scientific Computation (PETSc) Scalable Nonlinear Equations Solvers (SNES) interface [4]. This process repeats until a level of convergence specified within the SNES solver. At each iteration, the block Jacobian matrices are set up using multiphenics [5], a python library that also facilitates the definition of boundary restricted variables within FEniCS, a feature necessary for dealing in our case with the surface concentration. We note that the surface chemical potential is tied with the definition of the corresponding bulk quantity, but the surface concentration is not.

4.6 FEniCS implementation details

Although many documents [40,45] provide FeniCS implementation details, it is still not trivial to deal with surface kinematics using FEniCS as several surface quantities have a rank deficiency. For educational purposes, we review few important mathematical definitions of surface quantities and then we provide their corresponding FEniCS definitions.

The surface unit tensor is defined by $\hat{I} = I - N \otimes N$, which can be interpreted as surface (idempotent) projection tensor, and surface deformation gradient can be obtained from surface projection of bulk deformation gradient $\hat{F} = \check{F}\hat{I}$. Similarly, the surface gradient is obtained by surface projection of the bulk gradient $\nabla_{\hat{X}}\mu = \nabla_{X}\mu\hat{I}$.

```
N  =  FacetNormal ( mesh )
I_bulk      =  Identity (3)
I_surf      =  I_bulk      -   outer (N , N )
F_surf      =  dot ( F_bulk , I_surf )
grad_mu_surf       =  dot ( grad ( mu ) , I_surf )
```

Note that the surface unit tensor $\hat{I}$ is absent from the (principal) normal component $N \otimes N$; as a result, surface projection always leads to a rank deficiency, and we cannot perform the inverse operations for the surface quantities. Nevertheless, they possess an inverse in the generalized sense, i.e., $\hat{F}^{-1} := \hat{I}\check{F}^{-1}$ and $\hat{C}^{-1} := \hat{I}\check{C}^{-1}\hat{I}$.

```
F_surf_inv        =  dot ( I_surf , inv ( F_bulk ) )
C_surf_inv        =  dot ( I_surf , dot ( C_bulk ,
    I_surf ) )
```

In addition, we cannot perform the determinant operation for the surface quantities due to rank deficiency. We formulate an alternative way of using Nanson's formula to obtain the determinant of surface quantities, i.e., $J^s = \det \mathbf{F}^s := |\mathrm{cof}\mathbf{F}\mathbf{N}|$.

```
A_surf      =  dot ( cofac ( F_bulk ) ,N )
J_surf      =  sqrt ( dot ( A_surf , A_surf ) )
```

5 Numerical examples

To study the performance of the suggested framework, we analyze the transient responses for two initial boundary value problems involving bulk and surface poroelasticity of hydrogels: (1) free contraction of a cube with smooth edges and (2) uniaxial tension of a cube with sharp edges. In both cases the edge length of the cubes is 10^{-3}m. In the following numerical study, we take the initial swelling ratio $\lambda_0 = 3.215$ and the Flory interaction parameter as $\chi = 0.2$. At room temperature $T = 298$K, we have $k_B T = 4 \times 10^{-21}$J/mol, and the representative value of the volume and area per molecule are $\Omega = 10^{-28}$m^3 and $A = 10^{-19}$m^2. In the absence of solvent molecules, the dry network has shear modulus $\mu = 4 \times 10^4$ N/m^2, which gives $N\Omega = 10^{-3}$ and $N_s A = 10^3$ [2]. The characteristic dimension and time scales are set as $H = 10^{-3}$m and $\tau = 1.0$ sec. Without loss of generality, we prescribe the following values for the parameters: $\beta = 1.0$, $\gamma = 1.0$, $\kappa = 10^3$ and $D/D = 1.0$.

For robustness of the numerical procedure, we follow a two-stage process. We initialize from a homogeneously swollen state, with initial homogeneous swelling stretch λ_0, neglecting elastic surface energy contribution. In the first stage, we ramp the surface energy linearly, from zero to its prescribed value, for the time interval $t/\tau \in [0.0, 1.0]$. This time interval is significantly smaller compared to the time the system needs for equilibration. Then in the second stage, we exponentially increase the time steps $\Delta t/\tau$ until equilibrium is attained, while holding the value of the surface energy fixed.

In Fig. 1, we illustrate the distinction between the dry network as the reference state (stress-free configuration) and the free-swollen network as the initial state. In cases of homogeneous swelling at the initial state, this initial configuration can be characterized by the initial deformation gradients $\mathbf{F}_0$ and $\mathbf{F}^s_0$, which arise due to the initial free-swelling with a swelling ratio of λ_0:

$$\mathbf{F}_0 = \lambda_0 \mathbf{I} \quad \text{and} \quad \mathbf{F}^s_0 = \lambda_0 \mathbf{I}^s \tag{49}$$

It is important to emphasize that our approach does not employ a decomposition of the deformation gradient in a manner similar to elastoplasticity, where separate constitutive assumptions are often made for individual components of the decomposition. While it is possible to decompose the deformation gradient using $\mathbf{F}_0$ for a direct relationship between the initial and current states, we instead, using the deformation gradient of the current state relative to the free swelling state [32], the deformation at the free swelling state (initial state) is chosen based on a homogeneous stretch λ_0, and from that point the deformation ensues.

The initial chemical potential μ_0 is derived by equating the stress expression from (33) to zero using the free swelling stretch λ_0, as outlined in previous works [31, 32]. This approach allows us to establish the initial chemical potential under the conditions of stress-free swelling,

$$N\Omega\left(\frac{1}{\lambda_0^3} + \ln\left(1 - \frac{1}{\lambda_0^3}\right) + \frac{1}{\lambda_0^3} + \frac{\chi}{\lambda_0^6}\right) = \Omega\mu_0 \tag{50}$$

We can obtain the initial free-swelling stretch $\lambda_0 = 3.215$ by setting the immersed condition $\mu_0 = 0.0$ [31]. We can also obtain the initial normalized surface concentration by numerically solving the normalized constitutive relation of Eq. (29d), which yields the initial value $c^s_0 = 0.3673$. It is important to note that the boundary of swollen hydrogel is assumed to be impermeable for the cases studies here, which is formulated by the flux boundary condition $J^s_0 = 0$ (see Eq. 14). That is, the species on the surface are not allowed to migrate into the exterior (environment). We note that for immersed conditions, we would need to assume local equilibrium instantaneously on the surface which would override the surface diffusion mechanism.

To investigate the numerical stability when time step is small ($\Delta t \to 0$), the block Jacobian matrix in Eq. (48) can be reduced to

$$\frac{\partial \mathbf{N}^I}{\partial \mathbf{d}^J} = \begin{bmatrix} \mathbf{K}^{uu}_{IJ} & \mathbf{K}^{u\mu}_{IJ} & \mathbf{K}^{uc}_{IJ} \\ \mathbf{K}^{\mu u}_{IJ} & \mathbf{K}^{\mu\mu}_{IJ} & \mathbf{K}^{\mu c}_{IJ} \\ \mathbf{K}^{cu}_{IJ} & \mathbf{K}^{c\mu}_{IJ} & \mathbf{K}^{cc}_{IJ} \end{bmatrix} \approx \begin{bmatrix} \mathbf{K}^{uu}_{IJ} & \mathbf{K}^{u\mu}_{IJ} & \mathbf{K}^{uc}_{IJ} \\ \mathbf{K}^{\mu u}_{IJ} & 0 & \mathbf{K}^{\mu c}_{IJ} \\ \mathbf{K}^{cu}_{IJ} & \mathbf{K}^{c\mu}_{IJ} & \mathbf{K}^{cc}_{IJ} \end{bmatrix} \tag{51}$$

where $\mathbf{K}^{\mu\mu}$ is proportional to time step (Δt), and it approaches zero at the short time limit. This indicates the saddle point problem structure inherently, which is known to lead to numerical oscillations; however, as the time progresses in the transient process, the parabolic nature of the diffusion equations regularizes the problem (see [58] Chapter 3 for the details of the saddle point problem of 3×3 block matrices). It is worth noting that this type of oscillations for the bulk poroelasticity problem, stemming from the inf-sup problem are known to be aleviated by several approaches including the choice of Taylor–Hood spaces (as shown for

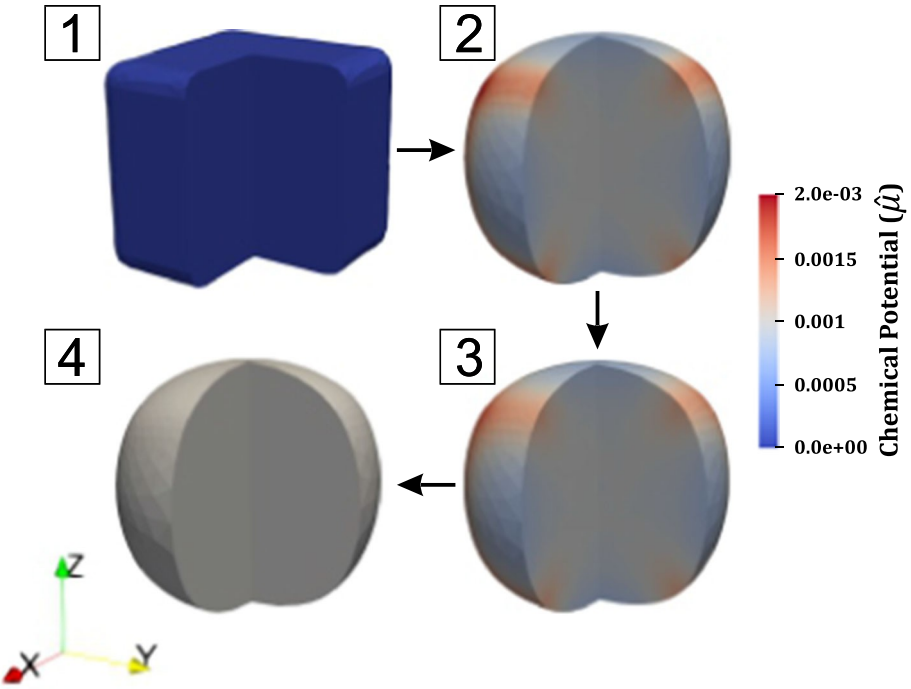

Fig. 2 Temporal sequence of the chemical potential during the free contraction of cubes

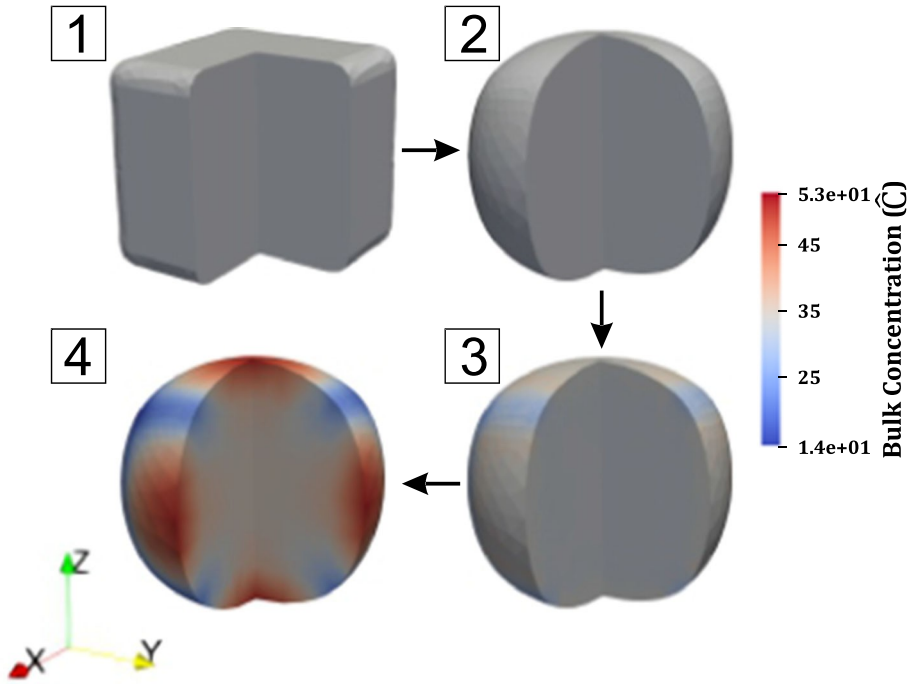

Fig. 3 Temporal sequence of the bulk contraction during the free contraction of cubes

the nonlinear problem in [13]. We have also chosen a Taylor–Hood space between the displacement and chemical potential, but also between the displacement and concentration.

5.1 Free contraction of a cube with smooth edges

In this example, we first investigate the surface and bulk poroelastic effects on a hydrogel cube. The cube is considered to be cast at a fully swollen state, and then released in an environment in which it is free to deform, but which cannot exchange solvent ($\hat{v}_p = 0$). For the finite element implementation of the free contraction of cubes, we use 3063 tetrahedral elements. The two-stage solution procedure detailed above is followed here.

We plot the temporal sequence of the finite element simulation for the chemical potential, bulk concentration, surface concentration, and surface flux in Fig. 2, 3, 4 and 5, respec-

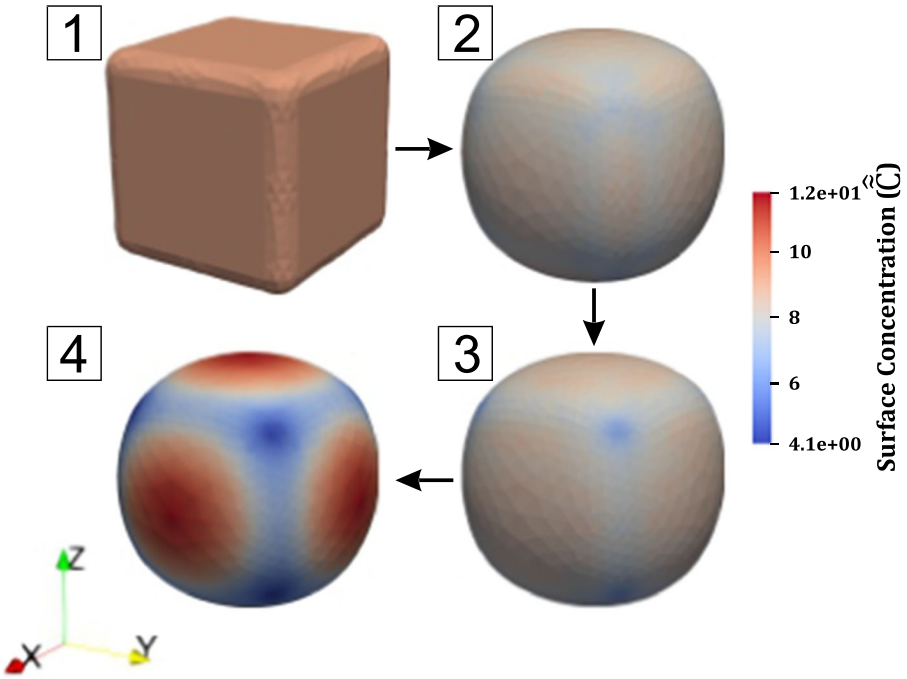

Fig. 4 Temporal sequence of the surface concentration during the free contraction of cubes

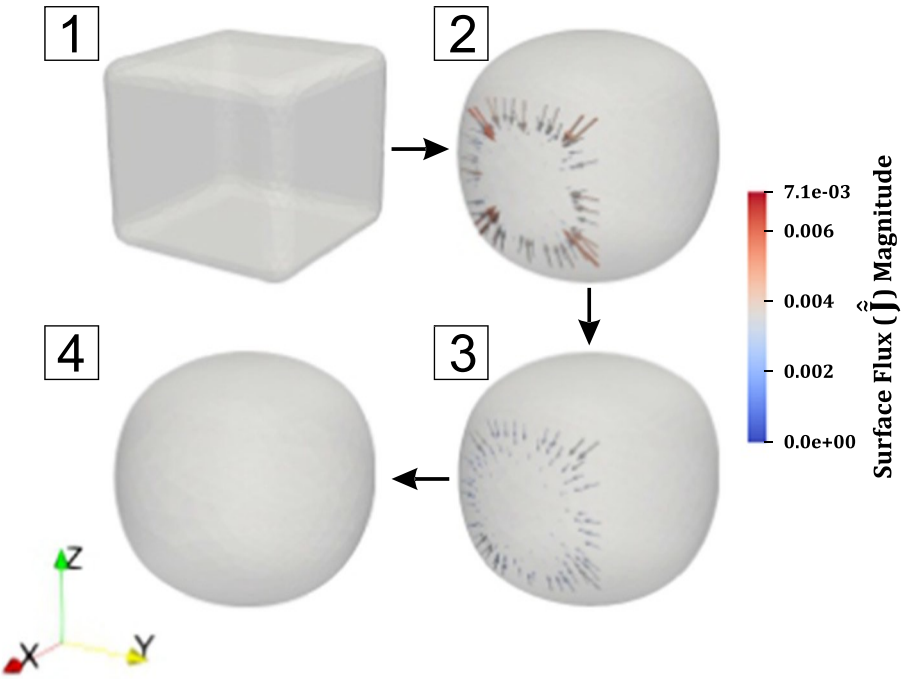

Fig. 5 Temporal sequence of the surface flux during the free contraction of cubes

tively, where all the values are normalized. We remove a quarter of the domain from the images of chemical potential in Fig. 2 and bulk concentration in Fig. 3 to show the contour plot on two sections of the interior along with the field on the surface. The surface flux in Fig. 5 is shown on only one face of the cube for visualization purposes. Images are taken at normalized time $t/\tau = 0.0, 1.0, 8.4, 7.8 \times 10^{4}, 7.8 \times 10^{6}$ in the clockwise, which are denoted by Step 1, 2, 3, and 4 in the following discussion. In Step 1 of Figs. 2 to 5, the cube are at the initial state by a homogeneous swelling stretch, $\lambda_0 = 3.215$. It is noteworthy that the cube is taken to have smooth edges (a case with sharp edges will be discussed in the following example).

Step 2 of Figs. 2 to 5 corresponding to the time steps the linearly ramping of the surface energy is included. This is for time $t/\tau = 1.0$ which is significantly smaller (4 orders of magnitude) compared to the equilibration time. We note that the current interpolation scheme leads to unstab

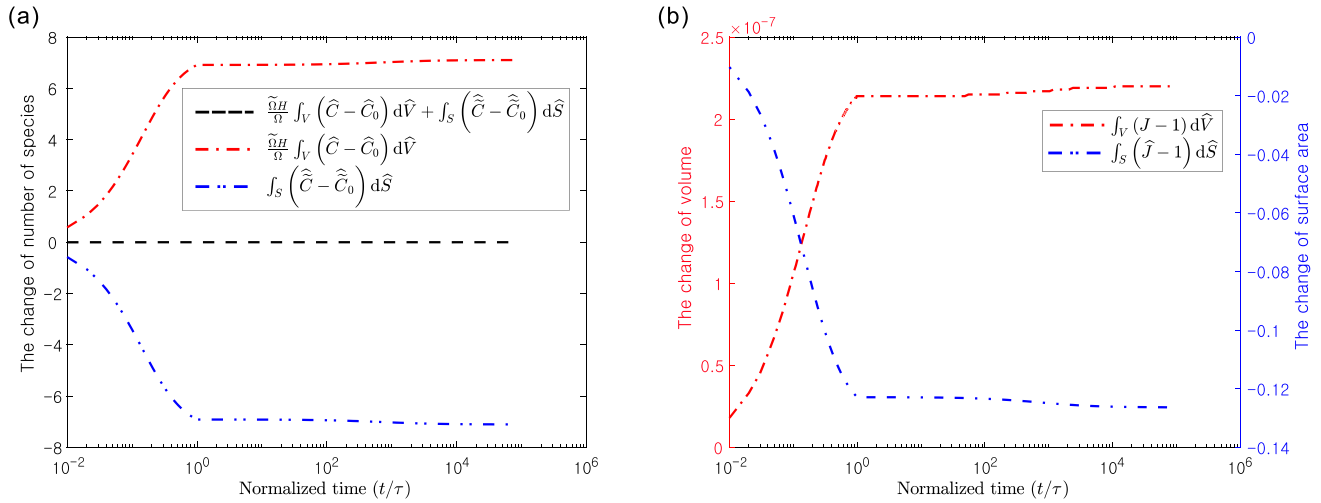

Fig. 6 Surface energy drives the species migration between the bulk and on surface. a The numbers of species in bulk and on surface are tracked with respect to the normalized time. b The change of volume and surface area are tracked with respect to the normalized time. During the surface energy ramping ($t/\tau \sim 1.0$), the bulk is gaining the species and the volume increases, while the surface is losing the species and surface area decreases. While surface energy is being fixed ($t/\tau > 1.0$), the bulk species still migrate from the surface into the bulk due to chemical potential. At equilibrium ($t/\tau \sim 1.6 \times 10^4$), there is no migration between the bulk and the surface. We note that the total number of species is constant at all times, and the volume increase of bulk is identical to the sum of the volume of species molecules moving into the bulk and the volume due to the incompressibility condition of Eq. (26)

results if the ramping time is significantly shorter, pointing to the need for the development of more advanced stabilization scheme in the future. This pathology might be a consequence of the three-field formulation. As the surface energy increases, the elastocapillary length becomes larger than the characteristic dimension H ; as a result, the surface effects become dominant that the geometry becomes almost spherical. In Step 2 of Fig. 2, the chemical potential is inhomogeneous due to the deformation driven by surface energy. In Step 2 of Figs. 3 and 4, the distribution of the bulk concentration on boundary is distinct from the surface concentration, and has not evolved as rapidly. This is owing to the fact that the species migration in bulk is slower than the one over surface, a specific modeling choice to highlight the lack of volumetric constraints for surface diffusion. However, at the equilibrium state, as shown in Step 4 of Figs. 3 and 4, the bulk distributions are similar on the surface.

On top of surface and bulk diffusion, in this system there is an exchange of species between the surface and the bulk, as captured in the strong form of the balance law for Eq. (14). The species exchange between bulk and surface is easily tracked by accounting for the molecular incompressibility condition of Eq. (26), indicating that the change of volume of the bulk is the same as the volume of the species migrating from bulk to surface. In Fig. 6, we track the normalized total species population in bulk and on surface at all time steps by integrating the normalized concentrations over the bulk and the surface accordingly. We can observe the species migration between $t/\tau = 0.0$ and 7.8×10^4. the total number of species is conserved. In Step 2 of Fig. the surface concentration is high near the smoothened ve of the cube because the deformation at that location is hig compared to the facet, which subsequently leads to higher chemical potential and species migration. In Step 2 of Fig. the surface diffusion is mainly directed from the edges to t interior of the facet. The direction of the surface diffusion governed by the surface deformation and chemical potent (see Eq. 41). Beyond Step 2, and for the rest of the transient respons the surface energy ($\tilde{\gamma} = 1$) is maintained at the same level, and we exponentially ramp the time steps towards equilib lack of. The deformation of the cubes is small beyond the in surface energy ramping, but the concentration (especially the bulk) significantly changes, driven by gradients of the chemical potential. In Step 3 of Figs. 3 and 4, we can see the diffusion in bulk and on surface, and the species migra the bulk to the interior of the facet of the cubes. In Step 4 of Fig. 2, the simulation reaches the equilibrium state, which is confirmed by the homogeneous chemical potential. The distribution of the bulk concentration on the boundary is similar to the surface concentration, as shown in Step 4 of Figs. 3 and 4. In Fig. 6, we can observe the significant migration between bulk and surface during ramping the su face energy ($t/\tau < 1$), but the migration between bulk and surface is negligible with surface energy being fixed ($1 < t/\tau \sim 7.8 \times 10^4$).

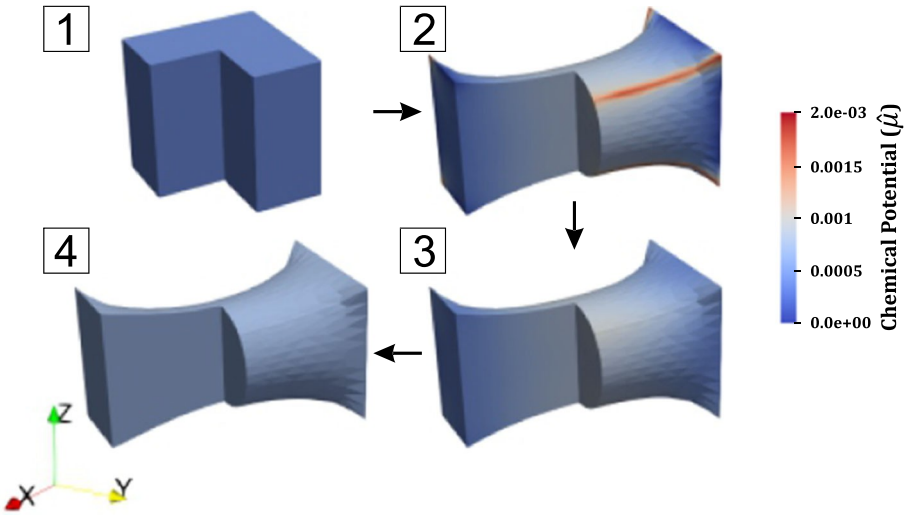

Fig. 7 Temporal sequence of the chemical potential during the tension of cubes

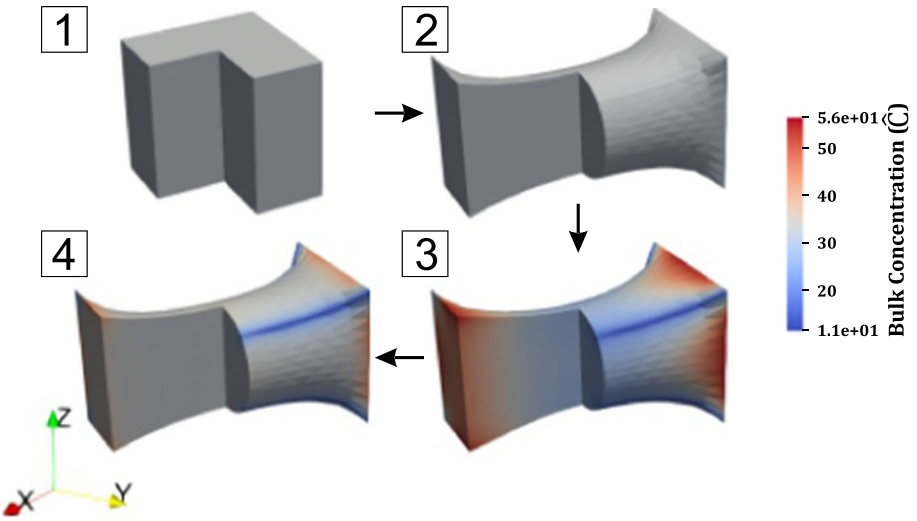

Fig. 8 Temporal sequence of the bulk contraction during the tension of cubes

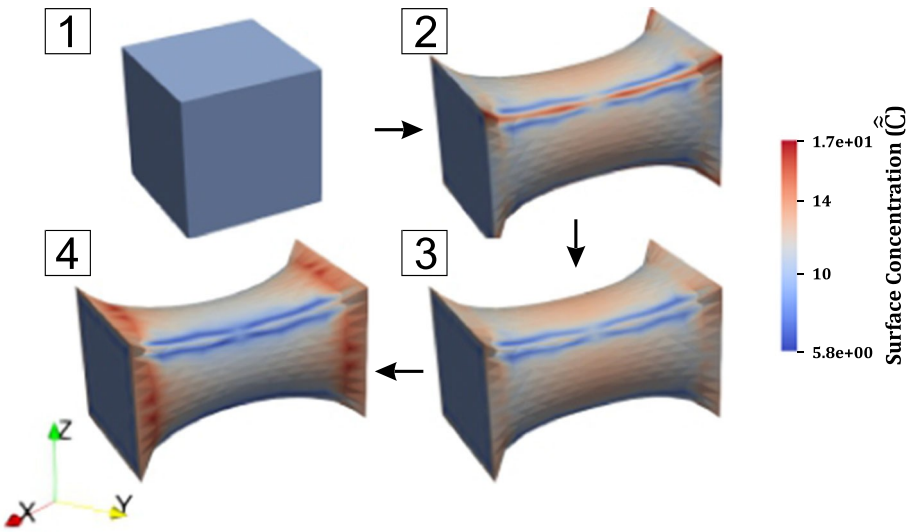

Fig. 9 Temporal sequence of the surface concentration during the tension of cubes

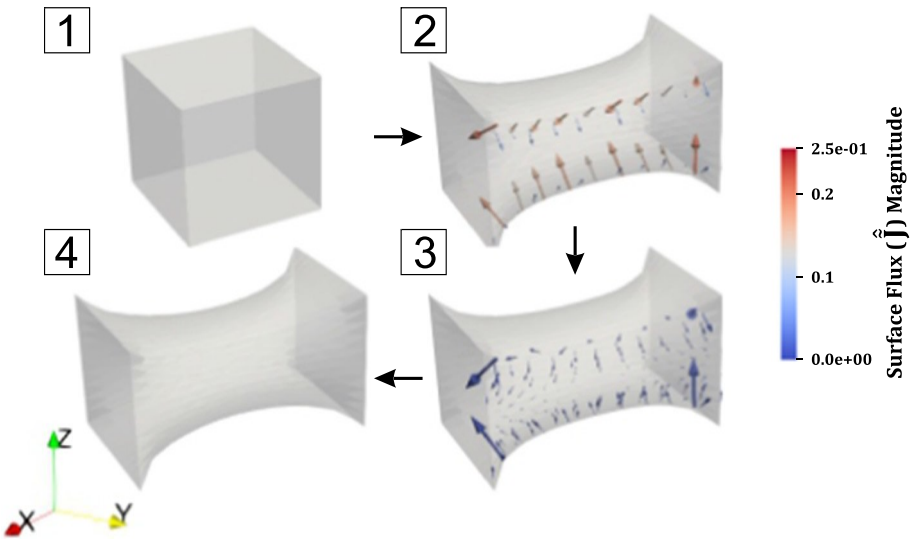

Fig. 10 Temporal sequence of the surface flux during the tension of cubes

5.2 Uniaxial tension of a cube with sharp edges

In this example, we first investigate the surface and bulk poroelastic effects on a hydrogel cube subject to external load. Similar to the previous example the cube is considered to be cast in a a fully swollen state, and released in an environment with which it cannot exchange solvent, and in this case it is subject to displacement controlled loading. The two-stage solution procedure detailed above is followed here as well. The lateral surfaces at $x = 0$, $y = \pm H/2$ are the clamped boundaries, and the others are free. For the displacement implementation of the tension of cubes, we use 1,029 tetrahedral elements. In this case, the displacement boundary conditions at lateral surfaces, are ramped linearly from zero in the same timeframe that ramping of the surface energy takes place.

In this case external mechanical loading along with surface and bulk energy contributions together dictate the resulting response of the system. The other conditions are the same as in the previous example of Sect. 5.1. We note that in this example, we have taken a cube geometry with sharp corners. We plot the temporal sequence of finite element simulations for the chemical potential, bulk concentration, surface concentration, and surface flux in Figs. 7 to 10, respectively, where all the values are normalized. The surface flux in Fig. 10 is shown on only one face of the cube for visualization purposes. Images are taken at normalized time $t/\tau = 0.0$, 1.0, 5.4×10^{-2}, 4.1×10^{0} in the clockwise, which are denoted by Step 1, 2, 3 and 4 in the following discussion.

In Step 1 of Figs. 7 to 10, the cubes are at the initial state by a homogeneous swelling stretch, $\vartheta = 3.15$. In Step 2 of Figs. 7 to 10, the cubes are deformed by the surface energy and stretch, after the initial load and surface energy ramping. The cubes are initially clamped at lateral sides, and we linearly ramp the surface energy $\breve{\gamma} = 1$ and stretch $\varepsilon = 68.9\%$ between $t/\tau = 0.0$ and 1.0. In Step 3 of Figs. 7 to 10, we maintain the surface energy and the stretch, and we exponentially ramp the time-step size towards equilibrium. In Step 4 of Figs. 7 to 10, the simulation approaches the equilibrium state. Through the second example, we can observe that the fluid concentration is distinct from the bulk concentration evaluated on the boundary.

Unlike the previous example in Sect. 5.1, the cube at initial state has the sharp corners to investigate the impact of such geometric features to the numerical scheme. We can observe an oscillation of the surface concentration near the edges in the 1,029 in Fig. 9, which is partially regularized with time, a consequent of the enforcement of an initial condition in a heat conduction problem. This originates from the weakly enforced continuity condition in Eq. (14d), which states that the net surface flux on the boundary curve (between the adjacent surface elements) is always balanced. Of course, this can easily be resolved (as in the previous example), where sharp features can be smoothened at the expense of computation, or moving to a finer non-structured mesh. Alternative, one could remark on deriving an appropriate stabilization scheme for this. We do not consider the impact of these initial oscillations to be significant to the transient response, similar to imposing discontinuous chemical potential boundary (with respect to the initial condition) for swelling of hydrogels [1]. Again, this might be specific to the three-field formulation, and a two-field formulation could also alleviate the issue.

6 Conclusion

A continuum multiphysics formulation and corresponding finite element implementation has been presented to account for bulk and surface nonlinear poroelasticity in hydrogels. The governing equations for the response of a continuum

body have been presented, and the general constitutive equations are derived in a thermodynamically-consistent manner, which is subsequently specialized for hydrogels. The proposed nonlinear theory is numerically solved through the mixed finite element method by employing the open-source finite element framework FEniCS. In addition, we provide FEniCS implementation details that could be important for problems where surface kinematics are of interest.

In our study, we assumed that the curve and vertex tensions and corresponding thermodynamic contributions [54], such as curve elasticity and diffusion in this context, are considered to be negligible compared to the bulk and surface effects. However, in cases involving contact, such as multiple hydrogel contacts, interfacial effects and curve thermodynamics would become important and should be considered for more accurate analyses, as demonstrated in previous works [37, 53, 54]. For the specific scenarios we investigated, the coupling of bulk and surface poroelasticity was the primary focus, allowing us to gain valuable insights into the multiphysics phenomena without the added complexity of considering curve and vertex thermodynamics contributions.

Two numerical examples are investigated to understand the effect of coupling bulk and surface poroelasticity. In the first example, where a cube with smoothened geometric features is investigated (see Figs. 2 to 6), we probe the variation of concentration, surface flux, and change of volume and surface area along with the chemical potential, which follow accounting for a fluid-like surface energy for the soft solid. As a result of the transient procedure and species exchange between bulk and surface, a smooth cube-like object is gradually transformed into an almost spherical one. From this observation, one may expect that the volume of the cube is decreased. Interestingly, the result is the opposite, as shown in Fig. 6. It implies that the species collectively migrate from the surface into the bulk because the volume increase of bulk is identical to the volume of total species moving into the bulk; consequently, the volume of the cube rather increases in spite of the surface area decreasing. This result suggests that the multiphysical complication could play an important role in understanding the responses of soft matter at length scales that surface effects dominate.

In the second example (see Figs. 7 to 10), we further investigate the response of a cube with sharp features, as external load, while still accounting for a fluid-like surface energy. Although the distributions of species concentration in bulk and on the surface are similar on the boundary in the first example (see Figs. 3 and 4), the second example showcases that the pathways of species migrations can be significantly different (see Figs. 8 and 9). In this example, we choose the same mobility constant in bulk and on the surface as the simplest case, but this result still provides an important insight into hydrogel-based applications at small scales. For example, one may use the distinct migration mechanism for the advanced design of hydrogel-based sensors and actuators.

Even though we focus on hydrogels in this work, the general framework and finite element implementation developed here can allow studying several problems for solids as well. In mechanobiology, where diffusion processes in the bulk and on the surface are coupled with the elastic response. One can adopt our numerical framework, but different constitutive relations must be specialized for studying other materials. A specific example that the authors plan to pursue is the modeling of morphogenic processes in tissue mechanics and, more specifically, modeling of contractile microtissues [38, 39, 49], where cells apply forces and contract the extracellular matrix (ECM), but at the same time can diffuse within the bulk of the ECM but also on its peripheral boundary, which has significant implications in problems like wound healing. In this paper, we report numerical issues that can arise due to several reasons and propose approaches to alleviate them. For authors' future work, it would also be interesting to extend our model to consider growth mechanisms to account for surface morphology in evolving natural systems, such as encountered during tumor growth.

Acknowledgements HK and NB acknowledge the support by the National Science Foundation under grant no. CMMI-2129776. CYH acknowledges the support by the National Science Foundation under grant no. CMMI-1903308. FB thanks the project "Numerical modelling of flows in porous media" funded by Universita` Cattolica del Sacro Cuore, and the INDAM-GNCS project "Metodi numerici per lo studio di strutture geometriche parametriche complesse" (CUP_E53C22001930001, PI Dr. Maria Strazzullo).

Declarations

Conflicts of interest The authors declare that they have no known competing financial interests or personal relationships that could have appeared to influence the work reported in this paper.

Appendix A: Derivation of weak form of species balance

Staring form Eq. (14a),

$$\int_V \dot{c}\,\delta\mu\,dV + \int_V (\nabla_X \cdot J)\,\delta\mu\,dV = 0 \tag{A1}$$

By applying the product rule and divergence theorem [29] and then substituting Eq. (14b) into Eq. (A1),

$$\int_V \dot{c}\,\delta\mu\,dV - \int_V J \cdot \nabla_X \delta\mu\,dV + \int_S \dot{c}\,\delta\mu\,dS + \int_S \nabla_X \cdot \hat{J}\,\delta\mu\,dS = 0 \tag{A2}$$

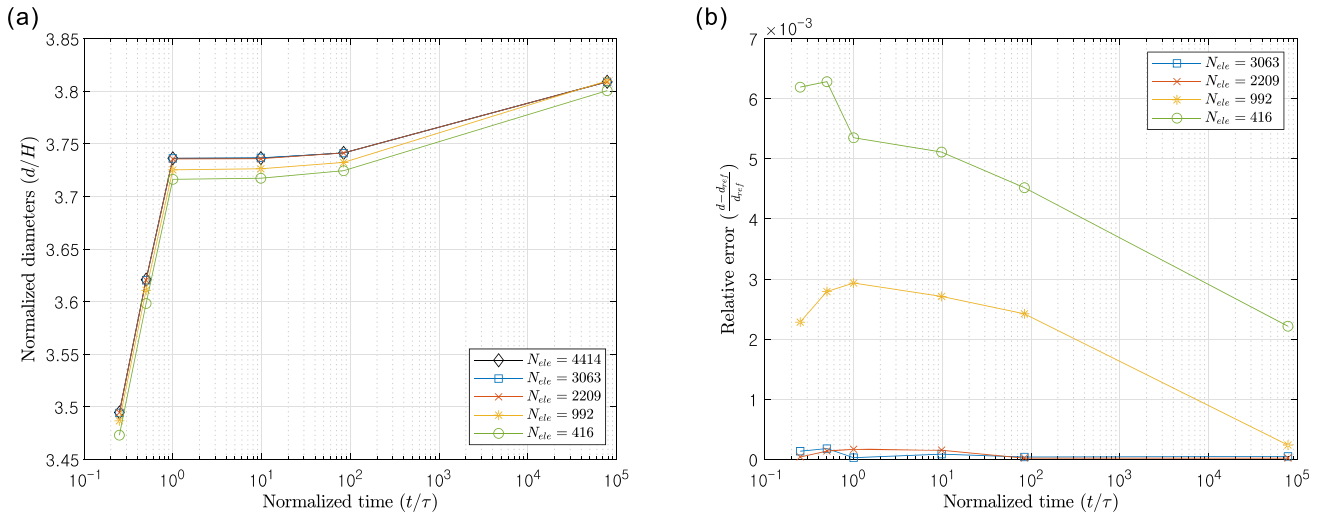

Fig. 11 The convergence study was performed with respect to different numbers of elements and normalized time for four different numbers of elements. The relative error with respect to normalized time is shown, with reference values obtained from the simulation using N ele = 4414 elements

where the last term in Eq. (A2) can be rewritten by product rule and surface divergence theorem,

$$\int_S \nabla_X \cdot \left(\frac{\partial \Psi}{\partial \mathbf{F}} \delta\mu\right) dS = -\int_S \frac{\partial \Psi}{\partial \mathbf{F}} \cdot \nabla_X \delta\mu \, dS + \int_L \frac{\partial \Psi}{\partial \mathbf{F}} \cdot \mathbf{N} \, \delta\mu \, dL \tag{A3}$$

where the second term in the right-hand side of Eq. (A3) is assumed to be zero. By substituting Eq. (A3) into Eq. (A2),

$$\int_V \dot{C} \, \delta\mu \, dV - \int_V \mathbf{J} \cdot \nabla_X \delta\mu \, dV + \int_S \dot{C} \, \delta\mu \, dS - \int_S \frac{\partial \Psi}{\partial \mathbf{F}} \cdot \nabla_X \delta\mu \, dS = 0 \tag{A4}$$

This equation corresponds to Eq. (34b) in the manuscript.

Appendix B: Convergence study on cube-contracting example

We perform the convergence study to demonstrate the simulation results and mesh resolution (see Fig. 11) on the contracting example in Sect. 5.1. During the surface energy ramping phase ($t/\tau < 1.0$), the bulk gains species, leading to a rapid increase in normalized diameters. While the surface energy is fixed ($t/\tau \geq 1.0$), the species continue to migrate from the surface into the bulk due to the chemical potential, resulting in a gradual increase in normalized diameter. The diameters stop increasing once the chemical potential reach equilibrium ($t/\tau \sim 1.6 \times 10^5$). It is important to note that the normalized diameters at multiple normalized times approach the reference values. Here we confirm a convergence of the solution following a global deformation metric.

References

1. Alnæs MS, Blechta J, Hake J et al (2015) The FEniCS project version 1.5. Archive of Numerical Software 3(100)
2. Ang I, Liu Z, Kim J et al (2020) Effect of elastocapillarity on the swelling kinetics of hydrogels. J Mech Phys Solids 145:104132
3. Babuška I (1971) Error-bounds for finite element method. Numerische Mathematik 16(4):322–333
4. Balay S, Abhyankar S, Adams M et al (2019) PETSc users manual
5. Ballarin F (2019) multiphenics—easy prototyping of multiphysics problems in FEniCS. https://github.com/multiphenics/multiphenics
6. Bathe KJ (2001) The inf-sup condition and its evaluation for mixed finite element methods. Comput Struct 79(2):243–252
7. Bico J, Reyssat É, Roman B (2018) Elastocapillarity: when surface tension deforms elastic solids. Annu Rev Fluid Mech 50:629–659
8. Biot MA (1955) Theory of elasticity and consolidation for a porous anisotropic solid. J Appl Phys 26(2):182–185
9. Biot MA (1956) Theory of propagation of elastic waves in a fluid-saturated porous solid II higher frequency range. J Acoust Soc Am 28(2):179–191
10. Biot MA (1962) Mechanics of deformation and acoustic propagation in porous media. J Appl Phys 33(4):1482–1498
11. Bleyer J (2018) Numerical tours of computational mechanics with Fenics. Zenodo
12. Bouklas N, Huang R (2012) Swelling kinetics of polymer gels: comparison of linear and nonlinear theories. Soft Matter 8(31):8194–8203
13. Bouklas N, Landis CM, Huang R (2015) A nonlinear, transient finite element method for coupled solvent diffusion and large deformation of hydrogels. J Mech Phys Solids 79:21–43
14. Brezzi F (1974) On the existence, uniqueness and approximation of saddle-point problems arising from Lagrangian multipliers. Publications mathématiques et informatique de Rennes S4:1–26
15. Cermelli P, Fried E, Gurtin ME (2005) Transport relations for surface integrals arising in the formulation of balance laws for evolving fluid interfaces. J Fluid Mech 544:339–351
16. Chester SA, Anand L (2010) A coupled theory of fluid permeation and large deformations for elastomeric materials. J Mech Phys Solids 58(11):1879–1906

17. Chester SA, Di Leo CV, Anand L (2015) A finite element implementation of a coupled diffusion-deformation theory for elastomeric gels. Int J Solids Struct 52:1–18
18. Dingreville R, Qu J, Cherkaoui M (2005) Surface free energy and its effect on the elastic behavior of nano-sized particles, wires and films. J Mech Phys Solids 53(8):1827–1854
19. Do Carmo MP (2016) Differential geometry of curves and surfaces: revised and updated, 2nd edn. Courier Dover Publications
20. Duda FP, Souza AC, Fried E (2010) A theory for species migration in a finitely strained solid with application to polymer network swelling. J Mech Phys Solids 58(4):515–529
21. Flory P (1961) Thermodynamic relations for high elastic materials. Trans Faraday Soc 57:829–838
22. Flory PJ (1942) Thermodynamics of high polymer solutions. J Chem Phys 10(1):51–61
23. Green AE, Zerna W (1992) Theoretical elasticity. Courier Corporation
24. Gurtin ME, Jabbour ME (2002) Interface evolution in three dimensions with curvature-dependent energy and surface diffusion: interface-controlled evolution, phase transitions, epitaxial growth of elastic films. Arch Ration Mech Anal 163:171–208
25. Gurtin ME, Murdoch AI (1975) A continuum theory of elastic material surfaces. Arch Ration Mech Anal 57(4):291–323
26. Gurtin ME, Murdoch IA (1978) Surface stress in solids. Int J Solids Struct 14(6):431–440
27. Gurtin ME, Fried E, Anand L (2010) The mechanics and thermodynamics of continua. Cambridge University Press
28. Henann DL, Bertoldi K (2014) Modeling of elasto-capillary phenomena. Soft Matter 10(5):709–717
29. Holzapfel GA (2000) Nonlinear solid mechanics II. Wiley
30. Hong S, Sycks D, Chan HF et al (2015) 3d printing of highly stretchable and tough hydrogels into complex, cellularized structures. Adv Mater 27(27):4035–4040
31. Hong W, Zhao X, Zhou J et al (2008) A theory of coupled diffusion and large deformation in polymeric gels. J Mech Phys Solids 56(5):1779–1793
32. Hong W, Liu Z, Suo Z (2009) Inhomogeneous swelling of a gel in equilibrium with a solvent and mechanical load. Int J Solids Struct 46(17):3282–3289
33. Huggins ML (1941) Solutions of long chain compounds. J Chem Phys 9(5):440–440
34. Javili A, Steinmann P (2009) A finite element framework for continua with boundary energies. Part I: the two-dimensional case. Comput Methods Appl Mech Eng 198(27–29):2198–2208
35. Javili A, Steinmann P (2010) A finite element framework for continua with boundary energies. Part II: the three-dimensional case. Comput Methods Appl Mech Eng 199(9–12):755–765
36. Javili A, McBride A, Steinmann P (2013) Thermomechanics of solids with lower-dimensional energetics: on the importance of surface, interface, and curve structures at the nanoscale. A unifying review. Appl Mech Rev 65(1):32
37. Javili A, McBride A, Steinmann P et al (2014) A unified computational framework for bulk and surface elasticity theory: a curvilinear-coordinate-based finite element methodology. Comput Mech 54(3):745–762
38. Kim J, Mailand E, Ang I et al (2020) A model for 3d deformation and reconstruction of contractile microtissues. Soft Matter 17:10198–10209
39. Kim J, Mailand E, Sakar MS et al (2023) A model for mechanosensitive cell migration in dynamically morphing soft tissues. Extreme Mech Lett 58(101):926
40. Langtangen HP, Logg A (2017) Solving PDEs in python: the FEniCS tutorial I. Springer
41. Leronni A, Bardella L (2021) Modeling actuation and sensing in ionic polymer metal composites by electrochemo-poromechanics. J Mech Phys Solids 148(104):292
42. Li B, Cao YP, Feng XQ et al (2012) Mechanics of morphological instabilities and surface wrinkling in soft materials: a review. Soft Matter 8(21):5728–5745
43. Li J, Mooney DJ (2016) Designing hydrogels for controlled drug delivery. Nat Rev Mater 1(12):1–17
44. Liu Z, Jagota A, Hui CY (2020) Modeling of surface mechanical behaviors of soft elastic solids: theory and examples. Soft Matter 16(29):6875–6889
45. Logg A, Mardal KA, Wells G (2012) Automated solution of differential equations by the finite element method: the FEniCS book vol 84. Springer, London
46. Logg A, Mardal KA, Wells GN (2012) Automated solution of differential equations by the finite element method. Springer
47. Lucantonio A, Nardinocchi P, Teresi L (2013) Transient analysis of swelling-induced large deformations in polymer gels. J Mech Phys Solids 61(1):205–218
48. MacMinn CW, Dufresne ER, Wettlaufer JS (2016) Large deformations of a soft porous material. Phys Rev Appl 5(4):044020
49. Mailand E, Li B, Eyckmans J et al (2019) Surface and bulk stresses drive morphological changes in fibrous microtissues. Biophys J 117(5):975–986
50. McBride A, Javili A, Steinmann P et al (2011) Geometrically nonlinear continuum thermomechanics with surface energies coupled to diffusion. J Mech Phys Solids 59(10):2116–2133
51. Murad MA, Loula AF (1994) On stability and convergence of finite element approximations of biot's consolidation problem. Int J Numer Methods Eng 37(4):645–667
52. Rastogi A, Dortdivanlioglu B (2022) Modeling curvature-resisting material surfaces with isogeometric analysis. Comput Methods Appl Mech Eng 401(115):649
53. Shi X, Liu Z, Feng L et al (2022) Elastocapillarity at cell-matrix contacts. Phys Rev X 12(2):021053
54. Steinmann P (2008) On boundary potential energies in deformational and configurational mechanics. J. Mech Phys Solids 56(3):772–800
55. Style RW, Jagota A, Hui CY et al (2017) Elastocapillarity: surface tension and the mechanics of soft solids. Ann Rev Condens Matter Phys 8:99–118
56. Taylor C, Hood P (1973) A numerical solution of the Navier-Stokes equations using the finite element technique. Comput Fluid 1(1):73–100
57. Treloar LG (1975) The physics of rubber elasticity
58. Wan J (2003) Stabilized finite element methods for coupled geomechanics and multiphase flow. Stanford University
59. Yoon J, Cai S, Suo Z et al (2010) Poroelastic swelling kinetics of thin hydrogel layers: comparison of theory and experiment. Soft Matter 6(23):6004–6012
60. Zhang J, Zhao X, Suo Z et al (2009) A finite element method for transient analysis of concurrent large deformation and mass transport in gels. J Appl Phys 105(9):093522